Experimental and numerical assessment of the effect of speed and loading conditions on the nominal wake of a containership

Carlo Giorgio Grlj[1]*, Nastia Degiuli[1], Ivana Martić[1]

[1]*University of Zagreb, Faculty of Mechanical Engineering and Naval Architecture, Ivana Lučića 5, Zagreb, 10000, Croatia*

ARTICLE INFO

ABSTRACT

An important aspect of the design of the propeller is the determination of the nominal wake. In this study, the nominal wake of a Post Panamax containership is determined numerically and experimentally at different speeds and loading conditions. The numerical simulations are based on the Reynolds averaged Navier Stokes equations, which are discretized using the finite volume method and the system of equations is closed using the Shear stress transport $k - \omega$ turbulence model. The nominal wake is determined with numerical simulations that model the effects of the free surface and without the free surface included, i.e., double body simulations. The verification study is conducted to assess the numerical uncertainty for the grid size and time step. The validation study includes a comparison of the contours of the dimensionless axial velocity component, the radial distributions of the circumferentially averaged dimensionless axial velocity components, and the integral values of the nominal wake. The effect of speed is more noticeable for the results obtained with EFD in comparison to the numerically obtained results, which is especially pronounced for the integral value of the nominal wake. The integral value of the nominal wake increases with the increase in the trim angle.

1. Introduction

The most important aspect of the propeller design is the nominal wake, which is measured at the propeller disc plane. The determination of the nominal wake is crucial for the propeller blade section design and local pitch, but also for the purpose of the efficiency evaluation of the Energy Saving Devices (ESD) [1]. Conventional methods for determining the full-scale nominal wake rely on the measured nominal wake at the model scale in the towing tank. However, due to the lack of validation studies, it is impossible to draw conclusions regarding the different wake field scaling procedures.

Significant scale effects on the nominal wake are present since it is strongly affected by viscous effects [2]. The scale effects are manifested through lower values of the axial velocity at the propeller disc plane at the model scale when compared to the full scale [3]. Zhang et al. [4] analysed the nominal wake in oblique flow using numerical simulations at model and full scale and showed a lower mean wake fraction at full-scale

---

numerical simulations compared to the model scale. The reason for this is that the nominal wake is largely affected by the viscous effects such as the relative thickness of the boundary layer which is larger at the model scale compared to the one at full scale. Similarly, Dogrul et al. [5] conducted numerical simulations of the viscous flow around the KRISO Containership (KCS) and the KRISO Very Large Crude Carrier 2 (KVLCC2) at different scales. The authors observed lower axial velocities on the propeller disc plane at lower Reynolds numbers and showed significant scale effects on the nominal wake. Pena et al. [6] investigated the aft end boundary layer and the wake of a full-scale general cargo ship using numerical simulations based on the Improved Delayed Detached Eddy Simulation (IDDES), which combines the Reynolds Averaged Navier-Stokes (RANS) and the Large Eddy Simulation (LES) approaches. It was found that the lower axial velocities in the nominal wake are caused by a negative pressure gradient and flow separation near the propeller.

Conventionally, towing tank tests are employed for the determination of the nominal wake at the model scale. Since measurements of the nominal wake are expensive and time-consuming, Computational Fluid Dynamics (CFD) at model and full scale is employed as an alternative. As shown by Farkas et al. [3], the scaling of the nominal wake is avoided by conducting numerical simulations of viscous flow around the full-scale ship, and consequently, the errors introduced by the scaling methods proposed by the International Towing Tank Conference (ITTC) are eliminated. The authors concluded that this is an important benefit of employing numerical simulations at full scale for the optimization of the stern flow and also for the validation of ESD performance. Pena et al. [7] pointed out that there is a lack of clear and concise guidelines for the investigation of the boundary layer around a full-scale ship. The authors investigated the effect of three turbulence models on the obtained boundary layer and nominal wake of a full-scale ship. The study showed that the lowest discrepancies between the numerical results and sea trial measurements are obtained using the IDDES approach. Alongside the determination of the nominal wake, it is important to assess the hull-propeller interaction [8, 9]. Sakamoto et al. [10] investigated the stern wake of two full-scale merchant ships using numerical simulations of the resistance and self-propulsion tests and showed that it is important to include the effects of surface roughness for the prediction of the nominal wake, total wake, and power.

The importance of taking into account surface conditions such as hard fouling or biofilm in the numerical simulations was pointed out by Farkas et al. [11]. The authors performed CFD simulations of the open water test to assess the impact of biofouling on the open water characteristics of the propeller and proposed a performance prediction method for fouled surfaces. It was concluded that further studies are needed to assess the impact of surface conditions on the propeller performance operating in the wake of the ship hull. The impact of soft fouling such as biofilm on the nominal wake was assessed by Farkas et al. [12] and it was shown that the integral value of the nominal wake of a bulk carrier can decrease by up to 7 % due to the presence of the biofilm.

Wang et al. [13] determined the scale effects on the nominal wake for the case of a 4000 TEU containership using CFD. The authors performed numerical simulations without considering the effects of the free surface, i.e., Double Body Simulations (DBS). The results obtained with DBS were compared to those obtained with Free Surface Simulations (FSS). The authors showed the negligible effect of the free surface on the nominal wake. However, the dependence of the mean axial wake on the Reynolds number was shown and a new method for scaling the nominal wake was proposed. Shin et al. [14] conducted a numerical investigation of the nominal wake in regular head waves for the KVLCC2 at the model scale for the full loading condition. The axial mean velocities in short wave conditions showed similar trends as in calm water. On the other hand, the significant impact of the large vertical motions on the nominal wake was shown in medium and long wave conditions. Mikkelsen et al. [15] indicated fluctuations in the nominal wake fraction of up to 39 % of the mean nominal wake fraction due to the large vertical motions of a KCS containership sailing in waves. Dai et al. [16] investigated the impact of head and oblique waves on the propulsive factors using CFD and obtained a decrease in wake fraction, hull efficiency, and propulsive efficiency in oblique waves in comparison to calm water conditions. Farkas et al. [17] assessed the scale effects on the wave resistance of a tanker and pointed out the importance of implementing a scaling procedure for the wave resistance coefficient in the existing extrapolation procedures.

Sun et al. [18] performed numerical simulations of the self-propulsion test for a commercial bulk carrier and showed the importance of determining the scale effects on the effective wake. The authors showed that modelling of the free surface as well as including the surface roughness can have a significant impact on the determination of the delivered power. Guo et al. [19] studied the scale effects on the nominal wake of the KCS model by modifying the aft hull to obtain a wake field similar to the one of the full-scale ship. The results were validated using the particle image velocimetry and the authors proposed a new method for eliminating the errors due to the scale effects on the nominal wake. Can et al. [20] determined the effective wake with numerical simulations of the self-propulsion test by using geometrically similar models within the CFD simulations to predict the effective wake at full scale. The proposed method showed better agreement of the obtained effective wake fractions with the results obtained by full-scale CFD simulations in comparison to those obtained using the ITTC 1978 extrapolation procedure.

Numerous studies have been conducted to assess various effects on the nominal wake, such as the effects of scale, surface roughness, fouling conditions, wave heading, and turbulence model. However, to the best of the authors' knowledge, insufficient research has been carried out to assess the effects of speed and loading conditions on the nominal wake. In addition, a detailed insight into the circumferential distribution of the different velocity components at the propeller plane is rarely given in similar studies. Thus, the aim of this study is the experimental and numerical determination of the nominal wake of the Post Panamax 6750 TEU containership with an emphasis on the effect of speed and loading conditions on the nominal wake distribution. The effect of the free surface on the nominal wake is assessed by comparing the results obtained with DBS and FSS. The rest of the paper is organized as follows. Section 2 provides the mathematical background of the numerical simulations and experimental setup. The case study, numerical setup, and verification and validation studies are presented within the same section. The results are given in Section 3, discussing the impact of speed and loading conditions on the nominal wake distribution. Finally, in Section 4 the conclusions of the study are summarized, and a plan for future work is given.

2. Methods

2.1 Geometry

A Post Panamax 6750 TEU containership is used as a case study for the experimental and numerical assessment of the nominal wake [21]. Table 1 shows the main particulars of the Post Panamax 6750 TEU containership at full scale and model scale, while Figure 1 presents the body plan and the 3D model.

Table 1 Post Panamax 6750 TEU containership main particulars

| Main Particular	Full scale	Model scale
Scale λ	1	35.18
Length between perpendiculars L_{PP}, m	286.60	8.147
Length overall L_{OA}, m	303.98	8.641
Breadth at waterline B_{WL}, m	40.00	1.137
Draught T, m	11.98	0.341
Displacement volume ∇, m3	85 634	1.967
Roll radius of gyration k_{xx}, m	14.60	0.415
Pitch radius of gyration k_{yy}, m	70.144	1.994
Yaw radius of gyration k_{zz}, m	70.144	1.994
Longitudinal centre of gravity (from AP) x_{CG}, m	138.395	3.934
Vertical centre of gravity z_{CG}, m	16.562	0.471
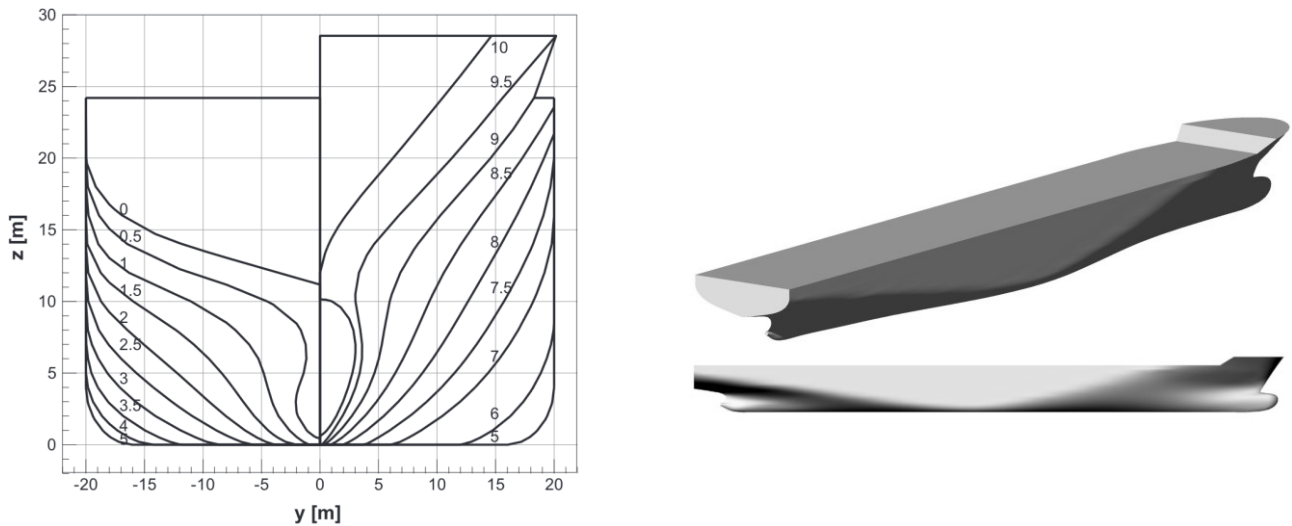
Fig. 1 The body plan and the 3D model of the Post Panamax 6750 TEU containership

The experimental and numerical investigations were performed for the ship at even keel at speeds of 19.95 kn and 16.02 kn, while for a ship trimmed by stern with a trim angle of -0.5° at 19.95 kn, corresponding to the full-scale ship. The loading conditions were defined by varying the trim while maintaining the same displacement volume as shown in Table 2. An additional numerical simulation was conducted at 23.94 kn, corresponding to the full-scale ship, for the assessment of the effect of speed on the nominal wake. The two speeds of 16.02 kn and 23.94 kn were selected as ±20 % of the design speed which is equal to 19.95 kn.

Table 2 Investigated loading conditions of the containership model

	Trim by stern		Even keel	Trim by bow	
Trim angle θ_S, °	−0.5	−0.25	0	0.25	0.5
Length of waterline L_WL, m	8.294	8.301	8.314	8.199	8.112
Draught at midship T_M, m	0.337	0.339	0.341	0.341	0.342
Draught at aft perpendicular T_A, m	0.372	0.354	0.341	0.326	0.313
Draught at forward perpendicular T_F, m	0.303	0.322	0.341	0.359	0.377

2.2 Experimental setup

An extensive experimental campaign was conducted at the Brodarski Institute in Zagreb for the case of the Post Panamax 6750 TEU containership [22], including resistance, open water, and self-propulsion tests and the measurements of the nominal wake at model scale $\lambda = 35.18$.

Model tests were performed in a large towing tank with a length of 276 m, a width of 12.5 m, and a depth of 6 m. It is equipped with a towing carriage with a maximum speed of 14 m/s. The wake measurements were performed using the five-hole Prandtl Pitot tube, shown in Figure 2. The axial v_A, radial v_R, and tangential v_T velocity components were calculated based on the difference between the measured absolute and static pressures in axial, radial, and tangential directions. The five-hole Prandtl Pitot tube was attached to a support extending from the stern tube, with the tube head positioned on the propeller disc plane 0.1112 m in front of the aft perpendicular. The velocity components were measured at multiple radial positions corresponding to $0.34R$ (0.035 m), $0.53R$ (0.055 m), $0.72R$ (0.075 m), $0.92R$ (0.095 m) and $1.01R$ (0.105 m). At each radial position, the velocity components were measured at angular positions in the range from 0° to 350° with 10° increments. The angular position of 0° corresponds to the bottom position of the tube, 90° to the starboard, 180° to the position of the tube vertically upwards, and 270° to the port side.

The towing speed was defined as 19.95 kn corresponding to the full-scale ship. A lower speed of 16.02 kn was selected for the even keel loading condition to assess the effect of ship speed on the nominal wake. The temperature of the water during the wake measurements was 13.7°C, the density 999.2 kg/m³, the kinematic viscosity 1.179·10⁻⁶ m²/s, and the respective dynamic viscosity 0.001178 Pa·s. It should be noted that the five-hole Prandtl Pitot tube is an intrusive method for measuring the velocity components since the instrument has to be placed within the measuring domain. As such, it can introduce disturbances in the flow field, and thus it is important to use a measuring device with low uncertainty. In its long-term practice, Brodarski Institute has developed reliable calibration procedures for measuring devices and in that regard has gained confidence in its experimental results. The uncertainty of the Prandtl Pitot tube is within the range of ±3 %.

Fig. 2 Five-hole Prandtl Pitot tube mounted behind the stern of the containership model

2.3 Mathematical model

The mathematical model used in the numerical simulations is based on the RANS equations. The governing equations arise from the conservation of mass and momentum laws. For the incompressible and unsteady case, the governing equations read as follows:

$$\frac{\partial \overline{u}_i}{\partial x_i} = 0 \tag{1}$$

$$\rho \frac{\partial \overline{u}_i}{\partial t} + \rho \frac{\partial}{\partial x_j}\left(\overline{u}_i \overline{u}_j + \overline{u_i' u_j'} \right) = -\frac{\partial \overline{p}}{\partial x_i} + \frac{\overline{\tau}_{ij}}{\partial x_j} \tag{2}$$

where ρ is the fluid density, $\overline{u}_i$ is the averaged Cartesian components of the velocity vector, $\rho \overline{u_i' u_j'}$ is the Reynolds Stress Tensor (RST), $\overline{p}$ is the mean pressure, and $\overline{\tau}_{ij}$ is the mean viscous stress tensor defined by:

$$\overline{\tau}_{ij} = \mu \left(\frac{\partial \overline{u}_i}{\partial x_j} + \frac{\partial \overline{u}_j}{\partial x_i} \right) \tag{3}$$

where μ is the dynamic viscosity of the fluid. The Finite Volume Method (FVM) is used for the discretization of the RANS equations (1) and (2).

The obtained system of equations is unclosed and thus a turbulence model needs to be applied to solve the discretized RANS equations. In this study, the Shear Stress Transport $k - \omega$ (SSTKO) turbulence model is used since it was already proven to be a good compromise between the accuracy of the obtained results and the computational time needed for the assessment of the nominal wake [3, 18, 5]. The SSTKO is a turbulence model that solves two additional transport equations for the turbulent kinetic energy k and for the specific dissipation ω:

$$\frac{\partial}{\partial t}(\rho k) + \frac{\partial}{\partial x_i}(\rho k \bar{u}_i) = \frac{\partial^2 k}{\partial x_i^2}(\mu + \sigma_k \mu_t) + G_k + G_{nl} + G_b - \rho \beta^* f_{\beta^*}(\omega k - \omega_0 k_0) + S_k \quad (4)$$

$$\frac{\partial}{\partial t}(\rho \omega) + \frac{\partial}{\partial x_i}(\rho \omega \bar{u}_i) = \frac{\partial^2 \omega}{\partial x_i^2}(\mu + \sigma_\omega \mu_t) + G_\omega + D_\omega - \rho \beta f_\beta(\omega^2 - \omega_0^2) + S_\omega \quad (5)$$

where σ_k, σ_ω, β^* and β are model-depending coefficients, G_{nl} is the non-linear production term, f_β is the free-shear modification factor, f_{β^*} is the vortex-stretching modification factor, and k_0 and ω_0 are the ambient values that counteract turbulence decay.

2.4 Numerical setup

For this study, two types of numerical simulations were conducted at model scale using the commercial software package STAR-CCM+ [23]. The first type is the DBS, where the symmetry boundary condition is applied at the waterline surface, while the second type is a numerical simulation that includes the effects of the free surface, i.e., FSS. The former is conducted following the ITTC recommendations [24] for the determination of the nominal wake for ships at low and moderate speeds. The Volume of Fluid (VOF) method is used in the FSS for locating and tracking the free surface. For the validation study, the Dynamic Fluid Body Interaction (DFBI) is used to model the ship motions by enabling two degrees of freedom, i.e., heave and pitch in the FSS simulations. Table 3 shows the overview of the conducted numerical simulations in this study. The numerical results are validated and compared to the experimentally obtained results for even keel at 16.02 kn and 19.95 kn and for a trim angle of -0.5° at 19.95 kn.

Table 3 Test matrix of the conducted numerical simulations

Speed, kn	$\theta_S = -0.5°$	$\theta_S = -0.25°$	$\theta_S = 0°$	$\theta_S = 0.25°$	$\theta_S = 0.5°$
16.02	/	/	DBS FSS	/	/
19.95	DBS FSS	FSS	DBS FSS	FSS	FSS
23.94	/	/	FSS	/	/

In both types of simulations, the computational domain consists of a rectangular box with the fixed bare hull of the containership embedded, which is discretized using an unstructured hexahedral mesh. It is assumed that the flow is symmetrical with respect to the symmetry plane of the ship and thus only half of the computational domain is created to lower the number of cells, and consequently to lower the computational time. The grid generation was performed carefully, paying attention to the discretization of the boundary layer. Wall functions were applied in both types of numerical simulations for solving the boundary layer. Thus, the dimensionless wall distance y^+ is maintained above 30 on the hull of the containership. To achieve the desired dimensionless wall distance, prism layers are created around the hull. The required distance from the wall to the centre of the first prism layer near the wall was estimated using the skin friction coefficient for a flat plate defined as:

$$C_f = 0.0576 Re^{-\frac{1}{5}} \quad (6)$$

The resulting equation for the determination of the distance between the wall and the centre of the first prism layer near the wall is defined as follows:

$$y = \frac{y^+ \nu}{\sqrt{0.0288 Re^{-\frac{1}{5}} v^2}} \qquad (7)$$

where ν is the kinematic viscosity of the water, Re is the Reynolds number, and v is the ship speed. Figure 3 shows the obtained dimensionless wall distance y^+ in the DBS and FSS. In both cases, the obtained dimensionless wall distance values are higher than 30 over the entire hull except for a small area in the stern region.

Dimensionless wall distance y^+

| 30 | 54 | 78 | 102 | 126 | 150 |
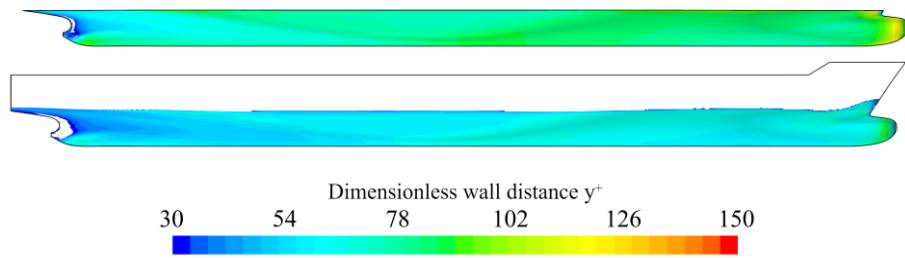
Fig. 3 The obtained dimensionless wall distance y^+ in the DBS (top) and FSS (bottom)

The generated grids vary depending on the ship speed and the type of simulations. In both FSS and DBS, the grid is refined near the hull with further refinements in the bow and stern regions. Special attention was given to the discretization around the propeller disc plane. Figures 4 and 5 show the detailed view of the generated grids for DBS and FSS, respectively. It should be noted that within the FSS, the expected locations of the free surface and the Kelvin wake were refined as well.

To further improve the stability of the FSS as well as to avoid wave reflections from the walls, the wave damping method is applied at the inlet, outlet, and side boundaries. The method was introduced by Choi and Yoon [25] and it introduces resistance to the vertical motion to dampen the waves near the boundaries to avoid their reflection. The resistance term is added to the equation for the vertical velocity component as follows:

$$S_z^d = \rho(f_1 + f_2 |w|) r^d w \qquad (8)$$

where f_1 and f_2 are parameters of the damping model, r^d is the damping strength indicator, w is the vertical velocity component, and ρ is the water density.

The computational domain consists of six boundaries which are placed far enough to avoid their effect on the obtained results following the ITTC recommendations [26]. The inlet and the side boundaries are placed at $1.5L_{PP}$ from the ship. The inlet velocity is applied at the inlet boundary and the symmetry boundary condition is applied at the side and symmetry boundaries. The outlet boundary is set at $3L_{PP}$ from the ship and constant pressure is applied in both DBS and FSS. The difference between the two types of numerical simulations is the selection of the boundary conditions of the top and bottom boundaries. In DBS, the top boundary is set at the waterline, and the symmetry boundary condition is applied at both the top and bottom boundaries, while in FSS the velocity inlet is set at the top and bottom boundaries. The bottom boundary is placed at $2L_{PP}$ from the ship and the top boundary in FSS at $1.5L_{PP}$ from the ship. The hull surface is assumed to be smooth, and the boundary condition is set as the no-slip wall. A detailed view of the computational domain with a focus on the boundary conditions and the main dimensions are shown in Figures 6 and 7 for the DBS and FSS, respectively.

The effect of numerical parameters on the obtained results was investigated by Grlj et al. [27] in detail. Based on this study, the first-order discretization scheme is chosen for the temporal discretization, while the

convection and gradient terms are solved using the second-order discretization scheme within the FSS [28]. Within DBS the temporal terms are not solved since it is a steady-state simulation.

It should be noted that the numerical simulations are performed for smooth hull and with the assumption of a fully developed turbulent flow in the whole computational domain. In the experimental study, a tripwire is placed in the bow region to stimulate the flow to become turbulent, thus forming a turbulent boundary layer around the hull.
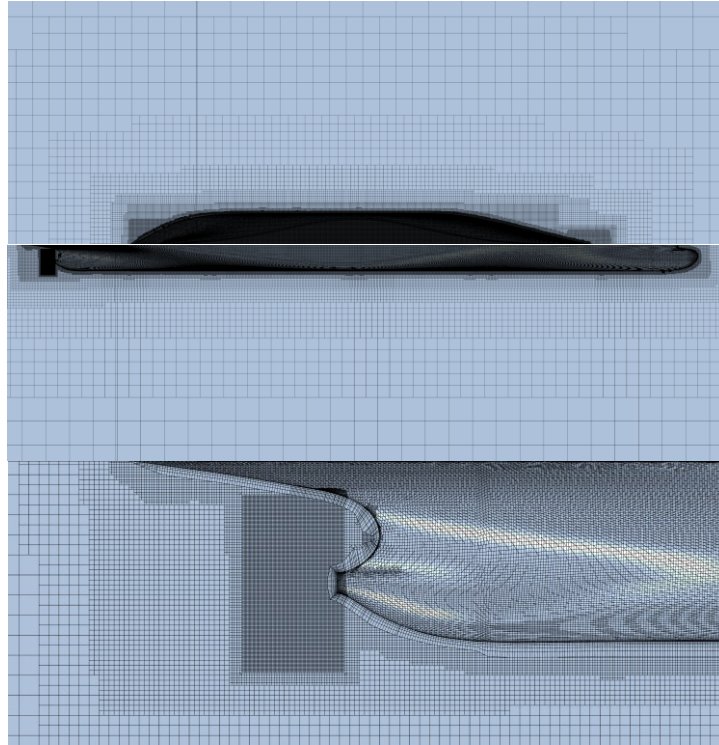
Fig. 4 Detailed view of the generated grids for the DBS
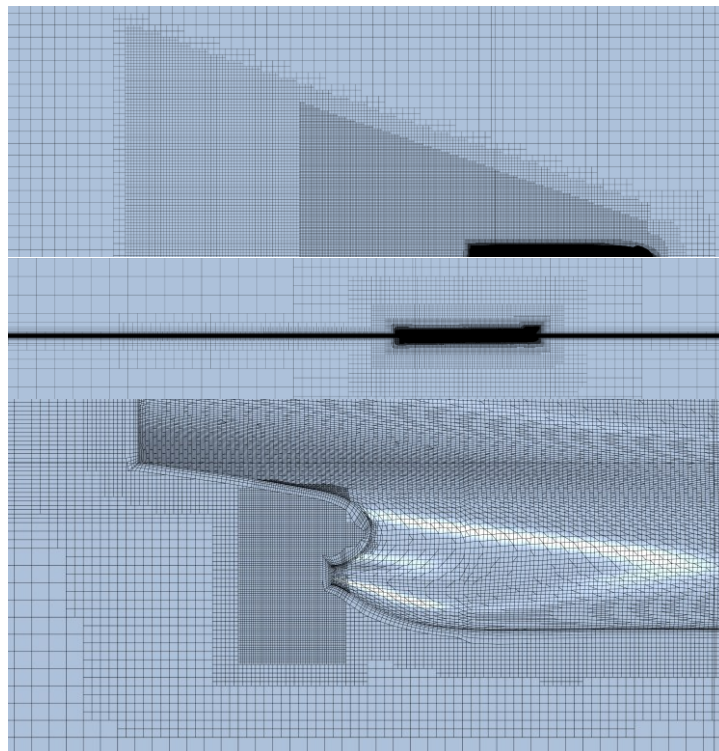
Fig. 5 Detailed view of the generated grids for the FSS
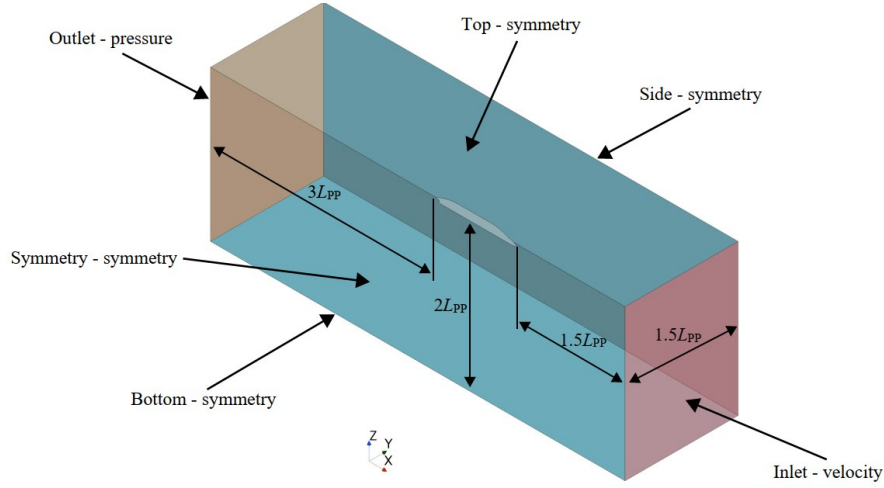
Fig. 6 Detailed view of the computational domain of the DBS with boundary conditions and main dimensions
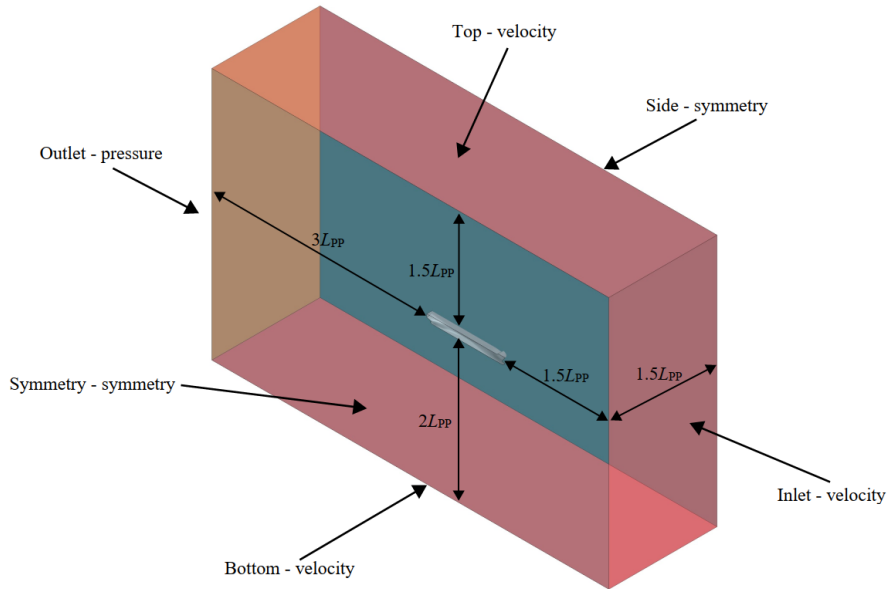
Fig. 7 Detailed view of the computational domain of the DBS with boundary conditions and main dimensions

2.5 Verification and validation studies

For the determination of the numerical simulation uncertainty, the Grid Convergence Index (GCI) method, as proposed by Celik et al. [29], is used. The apparent order of the method p is calculated using the following equation:

$$p = \frac{1}{\ln r_{21}} \cdot \left| \ln \left| \frac{\varepsilon_{32}}{\varepsilon_{21}} \right| + \ln \left(\frac{r_{21}^p - s}{r_{32}^p - s} \right) \right| \tag{9}$$

where r_{ij} is the grid refinement ratio, ε_{ij} is defined as $\varepsilon_{ij} = \phi_i - \phi_j$, with ϕ being the solution, and s is defined as $s = 1 \cdot \text{sgn}(R)$ with R being the discriminating ratio [30]. The discriminating ratio defines the convergence behaviour as:

1. Monotonic convergence: $0 < R < 1$,
2. Monotonic divergence: $R > 1$,
3. Oscillatory convergence: $R < 0$ and $|R| < 1$,

4. Oscillatory divergence: $R < 1$ and $|R| > 1$.

The order of the method p can be obtained by solving equation (9) using fixed-point iteration. The grid refinement ratio is calculated as the ratio between different grid spacings h:

$$r_{ij} = \frac{h_i}{h_j} \tag{10}$$

where h_i and h_j are calculated for each grid using the following equation:

$$h = \sqrt[3]{\frac{1}{N} \sum_{i=1}^{N} (\Delta V_i)} \tag{11}$$

where N is the total number of cells and V_i is the volume of the i-th cell. With the refinement ratio and the obtained order of the method, the extrapolated values can be calculated as:

$$\phi_{\text{ext}}^{21} = \frac{r_{21}^p \phi_1 - \phi_2}{r_{21}^p - 1} \tag{12}$$

The approximate relative error is calculated as follows:

$$e_{\text{a}}^{21} = \left| \frac{\phi_1 - \phi_2}{\phi_1} \right| \tag{13}$$

The extrapolated relative error is defined as:

$$e_{\text{ext}}^{21} = \left| \frac{\phi_{\text{ext}}^{21} - \phi_1}{\phi_{\text{ext}}^{21}} \right| \tag{14}$$

Finally, the grid convergence index is calculated with the following equation:

$$GCI_{\text{fine}}^{21} = \frac{1.25\, e_{\text{a}}^{21}}{r_{21}^p - 1} \tag{15}$$

For the purpose of the validation study, the relative deviations between the numerically obtained results (ϕ_{CFD}) and the measured values from the towing tank (ϕ_{EFD}) are calculated as follows:

$$RD = \frac{\phi_{\text{CFD}} - \phi_{\text{EXP}}}{\phi_{\text{EXP}}} \cdot 100\% \tag{16}$$

3. Results and Discussion

3.1 Verification study

Two verification studies were conducted for the grid size and one for the time step. The first verification study was performed for the grid size in the DBS. Two verification studies were conducted for the grid size and time step in the FSS. Details about the grids used in DBS and FSS can be found in Table 4 and Table 5, respectively. Both tables show the number of cells, grid spacings, and refinement ratios. In the verification study for the time step, a refinement ratio between the fine and medium, and coarse and medium time steps is

equal to two. The time steps were chosen according to the ITTC recommendations [26] for standard pseudo-transient resistance computations as $\Delta t = 0.005 \div 0.01 L_{PP} / U$.

Table 4 Grids used in the verification study of the DBS

Index	Number of cells N	Grid spacing h, m	Refinement ratio r_{ij}
1	4.5M	0.122	
			1.275
2	2.2M	0.156	
			1.462
3	0.7M	0.228	

Table 5 Grids used in the verification study of the FSS

Index	Number of cells N	Grid spacing h, m	Refinement ratio r_{ij}
1	3.5M	0.162	
			1.263
2	1.7M	0.204	
			1.385
3	0.6M	0.282	

Table 6 shows the obtained results of the verification study for the grid size in the DBS. It can be seen that the obtained numerical uncertainty is slightly below 4 %, which confirms that the fine grid is adequate for the numerical simulations. Monotonic convergence is achieved, and the order of method p is below 2 which may indicate that the obtained GCI is overpredicted.

Table 7 shows the results of the verification studies for the grid size and time step in the FSS. The results show that the monotonic convergence was achieved in both studies with the obtained GCI for the time step lower than 1 %. The obtained numerical uncertainty for the grid size is slightly higher than 4 % but the order of method p suggests that the GCI for the grid size is overpredicted. Nevertheless, the obtained numerical uncertainties are satisfactory and thus the fine grids are used in the remaining numerical simulations.

Table 6 Verification study for the grid size of the DBS

Parameter	Value
ε_{21}, N	-0.0036
ε_{32}, N	-0.0084
R	0.4301
p	1.2580
ϕ_{ext}^{21}, N	0.3385
e_{a}^{21}	0.0110
e_{ext}^{21}	0.0300
GCI_{fine}^{21}, %	3.87

Table 7 Verification study for the grid size and time step of the FSS

Parameter	Grid size	Time step
ε_{21}, N	-0.0040	-0.0050
ε_{32}, N	-0.0044	-0.0200
R	0.9091	0.2500
p	1.2990	2
ϕ_{ext}^{21}, N	0.3363	0.3267
e_{a}^{21}	0.0123	0.0154
e_{ext}^{21}	0.0336	0.0051
GCI_{fine}^{21}, %	4.35	0.64

3.2 Validation study

The results obtained with numerical simulations were compared with the towing tank measurements. The measurements were taken at five radii and at each radius the velocity was measured at 36 angles, covering the range from 0° to 360° with an increment of 10°. Figure 8 shows the measured velocity components for all loading conditions and speeds at different radial positions. These results were interpolated for the purpose of the validation study and the assessment of the effects of ship speed and loading conditions on the nominal wake.
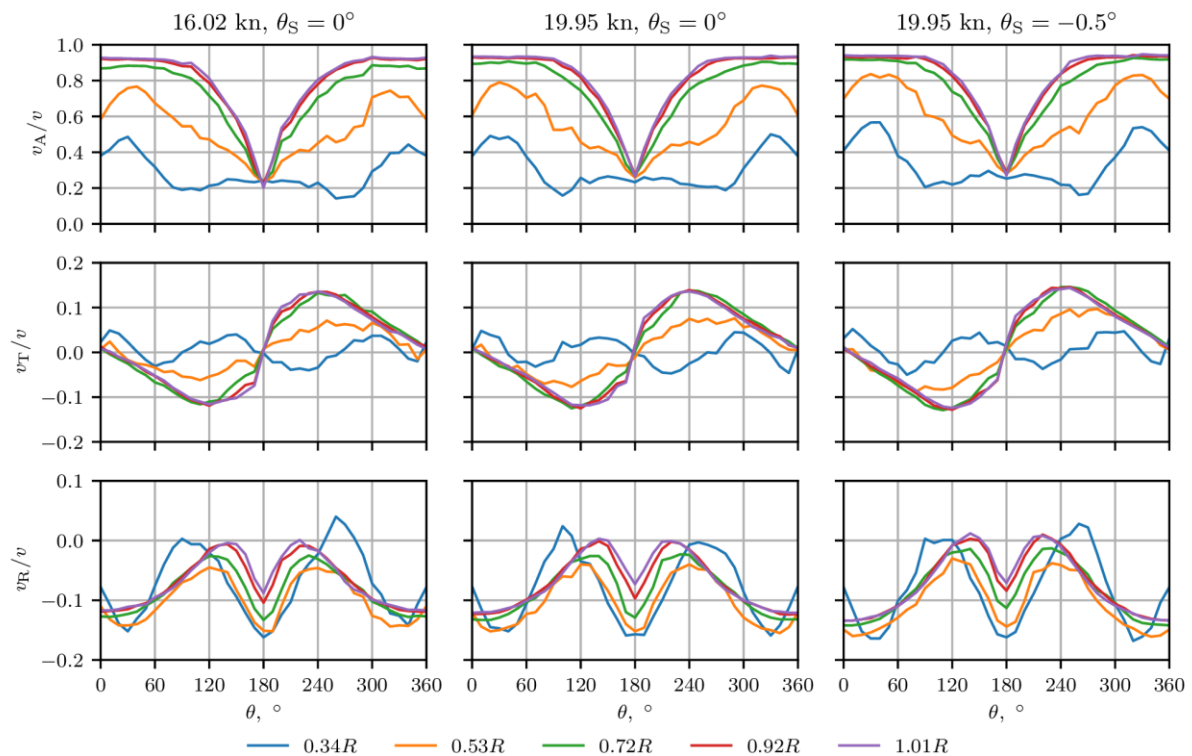
Fig. 8 Circumferential distribution of the axial (top row), tangential (middle row), and radial (bottom row) velocity components measured in the towing tank for even keel at 19.95 kn and 16.02 kn, and for a trim angle of -0.5° at 19.95 kn
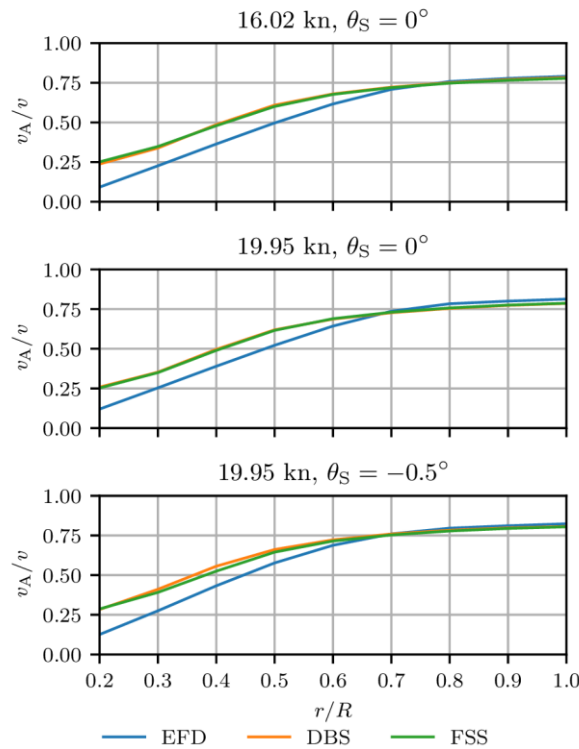
Fig. 9 The radial distribution of the circumferentially averaged dimensionless axial velocity components at different speeds and loading conditions

The radial distributions of the circumferentially averaged dimensionless axial velocity component were calculated at different radial positions and compared to the ones obtained with FSS and DBS as shown in Figure 9. It can be seen that the circumferentially averaged dimensionless axial velocity components are significantly overpredicted at radial positions from $0.2R$ to $0.6R$ for both loading conditions and ship speeds. The relative deviations decrease with the increase of the radius. The circumferentially averaged dimensionless axial velocity components are underpredicted for all loading conditions from $0.8R$ to $1.0R$. The highest and the lowest discrepancies are obtained with FSS for even keel at 16.02 kn and 19.95 kn, respectively.

Table 8 shows the results of the validation study for the integral values of the nominal wake. The relative deviations between the results obtained with Experimental Fluids Dynamics (EFD) and DBS, and EFD and FSS are presented. Lower discrepancies are obtained with FSS in comparison to DBS, especially for a trim angle of -0.5° at 19.95 kn and for even keel at 16.02 kn.

Table 8 The validation study for the integral values of the nominal wake

Speed, kn	θ_S , °	$w_{n, EFD}$	$w_{n, DBS}$	$w_{n, FSS}$	RD_{DBS} , %	RD_{FSS} , %
16.02	0	0.375	0.329	0.336	-12.27	-10.40
19.95	0	0.351	0.323	0.329	-7.98	-6.27
19.95	-0.5	0.326	0.288	0.298	-11.66	-8.59

3.3 Effect of speed

In this subsection, the nominal wakes obtained with EFD, FSS, and DBS at different speeds are compared. Figure 10 shows the contours of the dimensionless axial velocity component on the propeller disc plane obtained with EFD, FSS, and DBS at two speeds. It can be noticed that a larger wake peak in the region close to 180° at the speed of 16.02 kn was obtained by EFD in comparison to 19.95 kn. In addition, the velocity reduction is larger over the entire propeller disc plane for the speed of 16.02 kn. On the other hand, differences

between the dimensionless axial velocity components obtained for the analysed speeds were not captured entirely by DBS and FSS. The velocity reduction in the region close to the propeller hub obtained with FSS is larger than the one with DBS for both speeds. It can be seen that in the region close to the propeller hub, the EFD results show a higher velocity reduction in comparison to the results obtained numerically. The results obtained with FSS show better agreement with the EFD results than those obtained with DBS. Therefore, the remaining numerical simulations are carried out with the free surface effects included.

The contours of the dimensionless axial velocity component obtained with FSS at 16.02 kn, 19.95 kn, and 23.94 kn are shown in Figure 11. It can be noticed that the wake peak in the region close to 180° decreases with the increase in speed. The velocity reduction over the entire propeller disc plane is smaller as the ship speed increases.

Figure 12 shows the circumferential distribution of the dimensionless axial velocity component at different radial positions, while in Figures 13 and 14 the dimensionless tangential and radial velocity components are presented, respectively. In Figure 15 the differences between the dimensionless axial velocity components obtained at 16.02 kn and 19.95 kn with EFD can be seen at all radial positions. The numerical results show that these differences are present only at radial positions from $0.2R$ to $0.6R$. On the other hand, as can be seen from Figure 13 the differences between the dimensionless tangential velocity components obtained at 16.02 kn and 19.95 kn are negligible. The differences between the numerical results and those obtained by EFD can be noticed, especially at radial positions from $0.2R$ to $0.5R$. The differences between the dimensionless radial velocity components obtained numerically and by EFD are more pronounced than the other velocity components at all radial positions. The comparison between the circumferential distributions of the axial, tangential, and radial velocity components obtained with FSS at 16.02 kn, 19.95 kn, and 23.94 kn is presented in Appendix A.
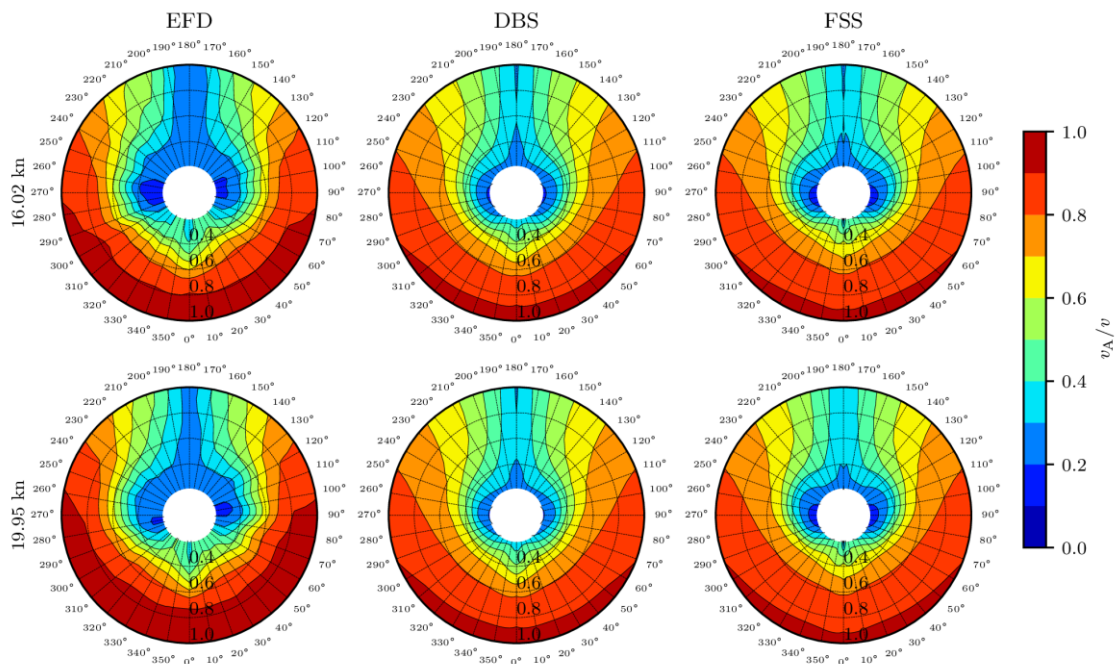

Fig. 10 Contours of the dimensionless axial velocity component on the propeller disc plane obtained with EFD, DBS, and FSS at different speeds
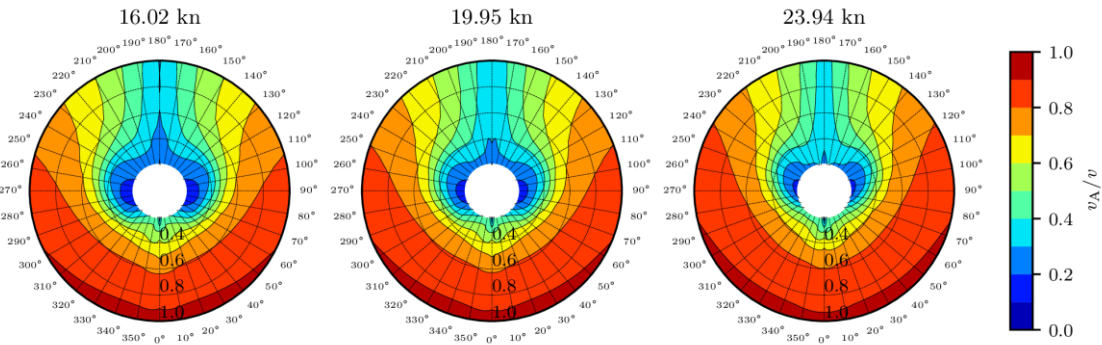
Fig. 11 Contours of the dimensionless axial velocity component on the propeller disc plane obtained with FSS at different speeds
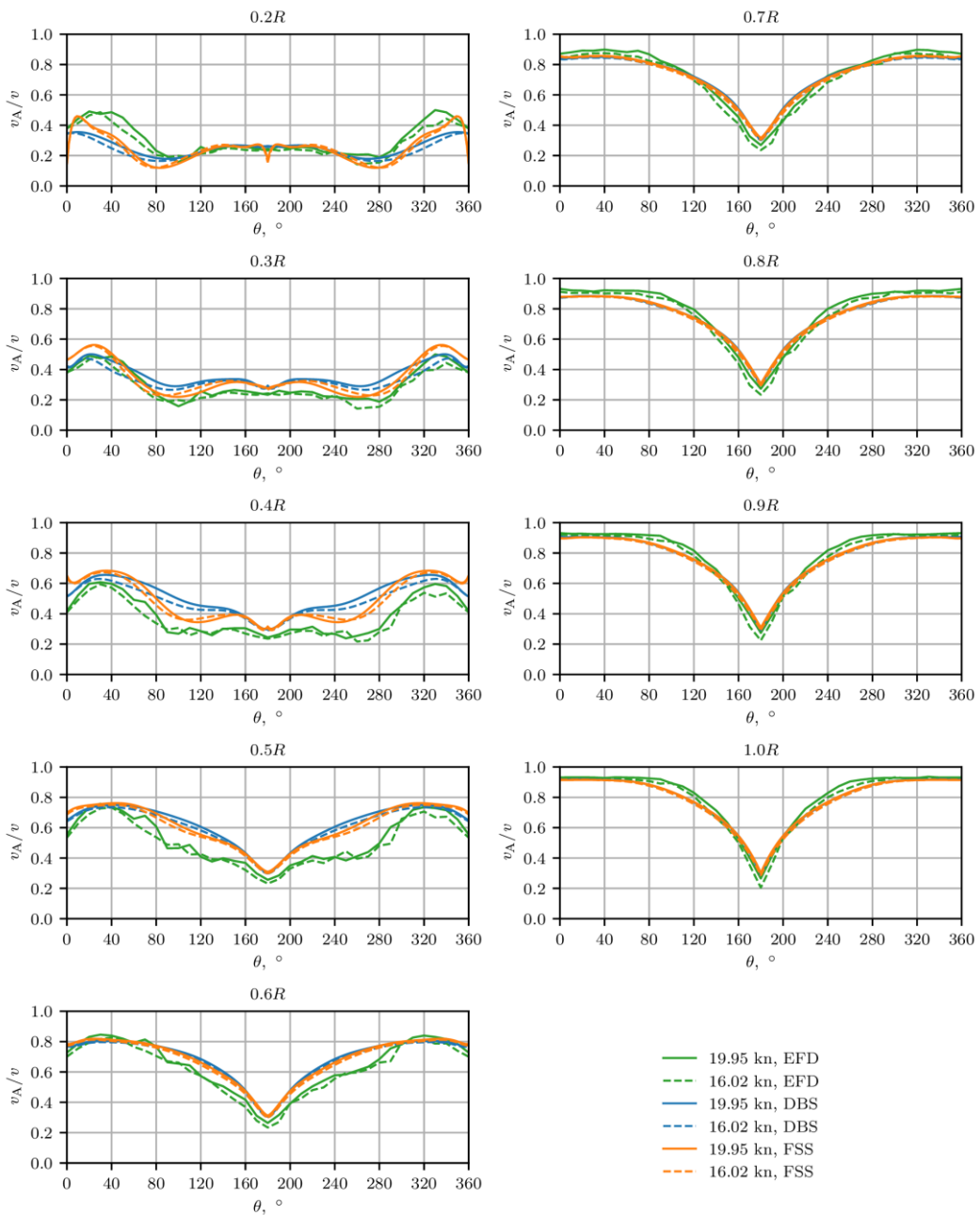

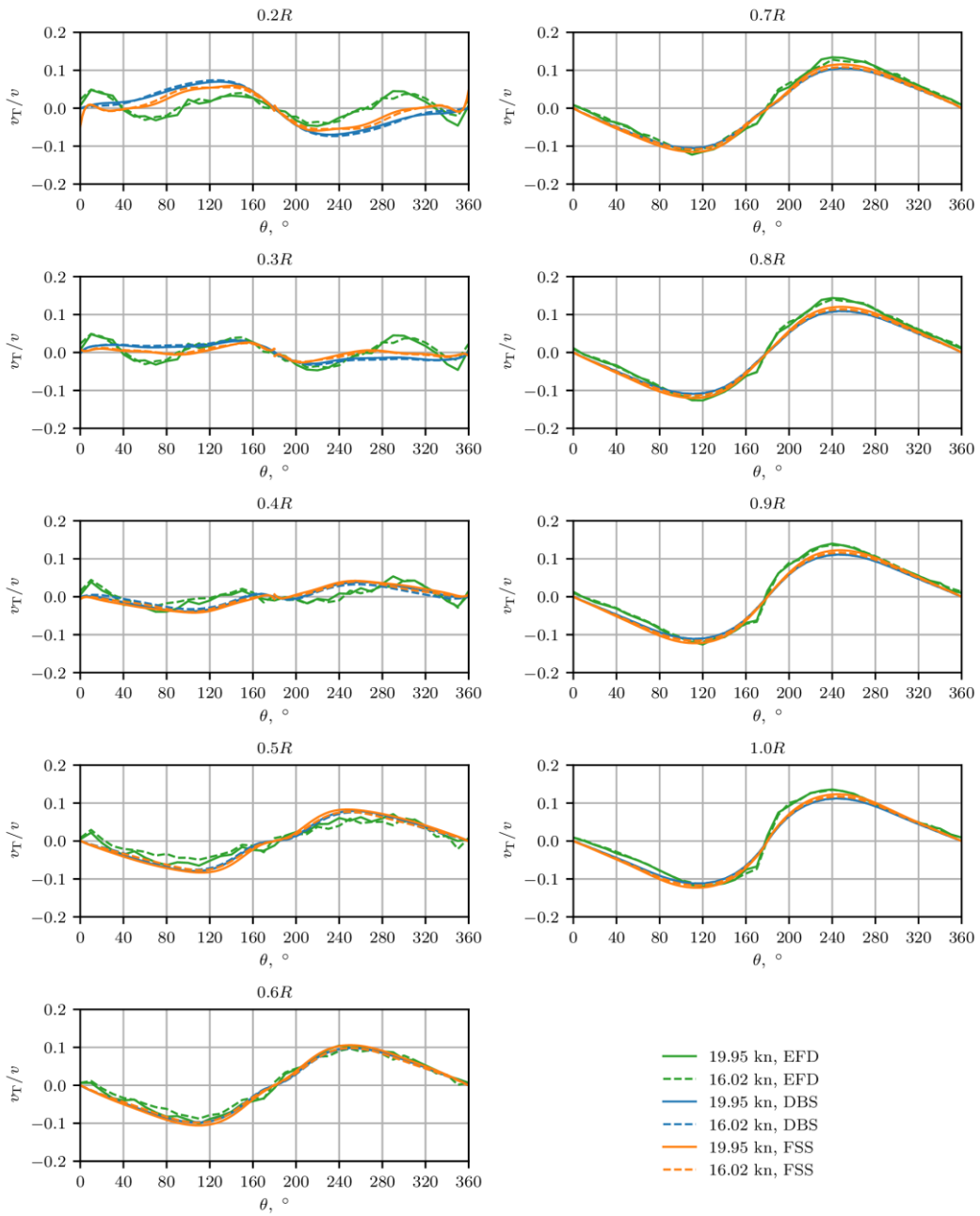**Fig. 12** Circumferential distributions of the axial velocity component for even keel at 19.95 kn and 16.02 kn

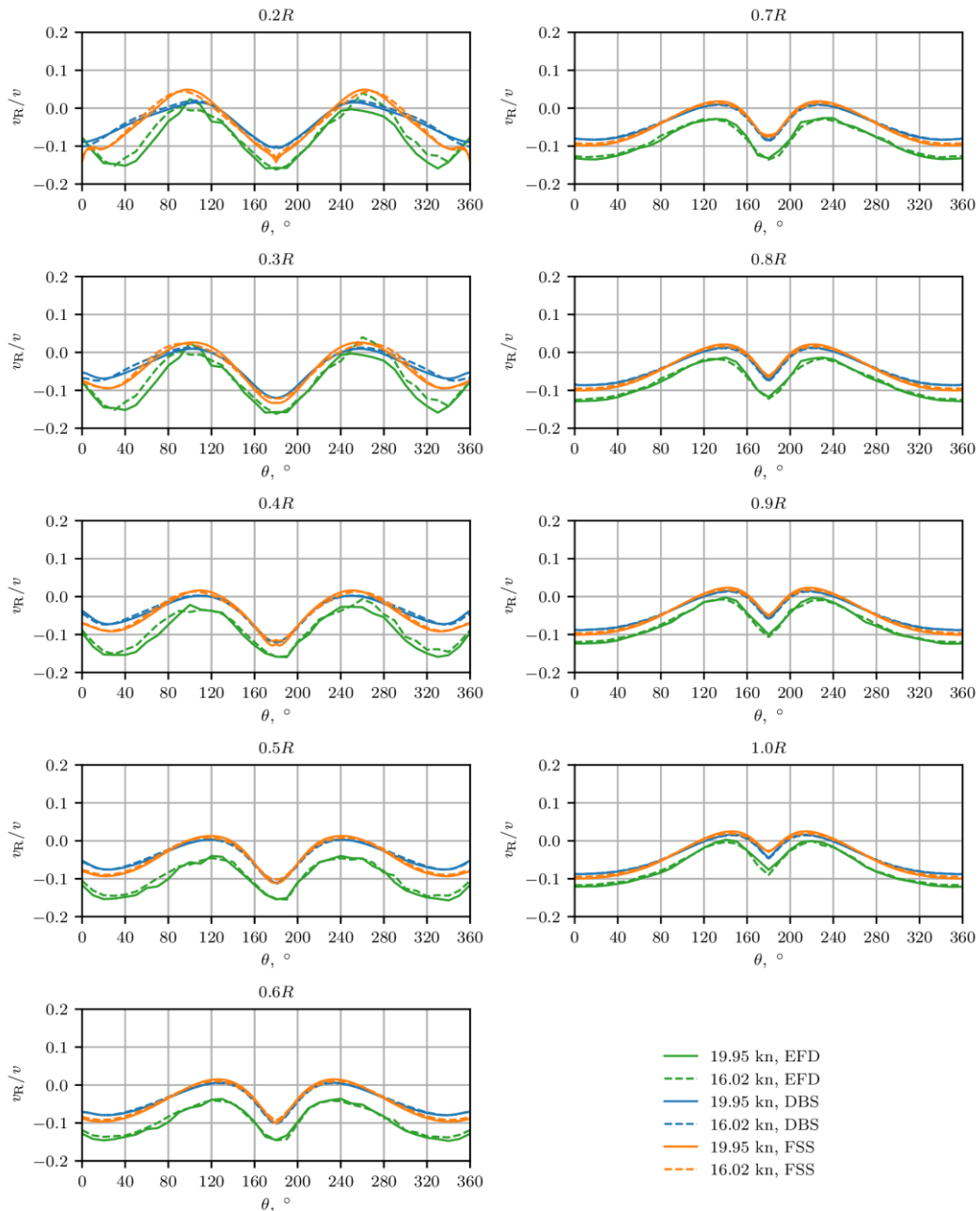**Fig. 13** Circumferential distributions of the tangential velocity component for even keel at 19.95 kn and 16.02 kn

Fig. 14 Circumferential distributions of the radial velocity component for even keel at 19.95 kn and 16.02 kn

The radial distributions of the circumferentially averaged axial velocity component obtained with EFD, DBS, and FSS at 19.95 kn and 16.02 kn are presented in Figure 15. A slight effect of speed on the circumferentially averaged axial velocity component can be seen, with the relative deviations obtained with DBS and FSS ranging from -0.4 % to -8 % and from -1 % to -7 %, respectively. The effect of speed is more noticeable for the results obtained with EFD with the relative deviations being in the range from -3 % up to 23 %. It should be noted that the relative deviations are calculated with respect to the results obtained at 19.95 kn. The relative deviations between the results obtained at the analysed speeds decrease with the increase of the radius. Figure 16 shows the obtained radial distributions of the circumferentially averaged axial velocity component obtained with FSS at 16.02 kn, 19.95 kn, and 23.94 kn. It can be seen that the relative deviations between the results obtained at 19.95 kn and 23.94 kn are larger than those obtained between 16.02 kn and 19.95 kn.
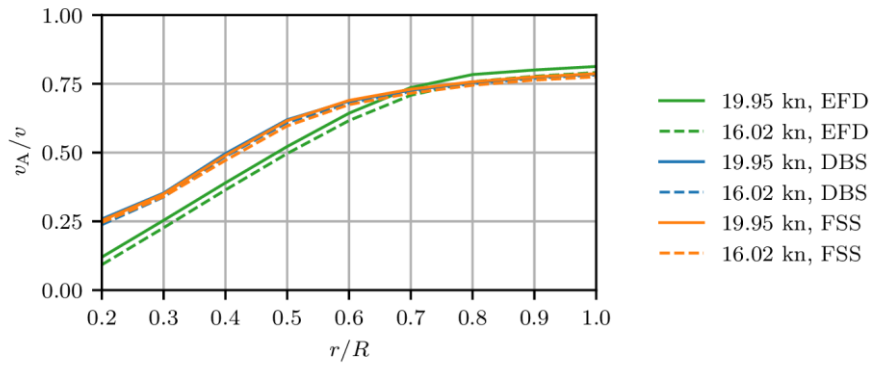
Fig. 15 Radial distributions of the circumferentially averaged dimensionless axial velocity component obtained with EFD, DBS, and FSS at 19.95 kn and 16.02 kn
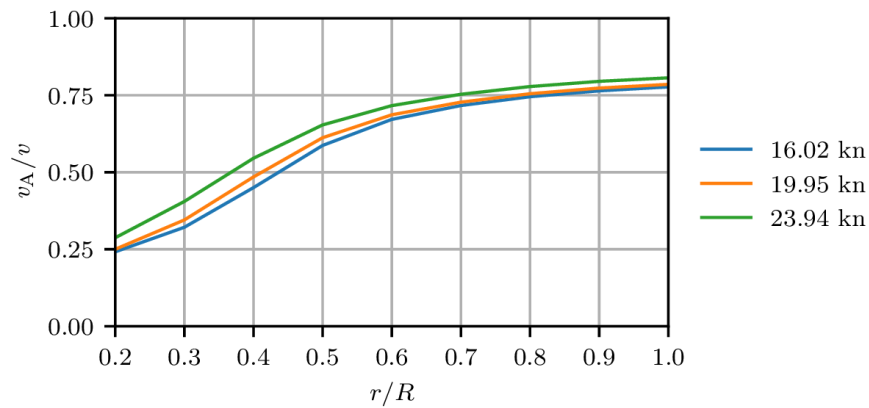

Fig. 16 Radial distributions of the circumferentially averaged dimensionless axial velocity component obtained with FSS at 16.02 kn, 19.95 kn, and 23.94 kn

The integral values of the nominal wake obtained with EFD, DBS, and FSS for even keel at 16.02 kn and 19.95 kn, and with FSS at 23.94 kn are calculated as the average value of the dimensionless axial velocity component on the propeller disc plane, Table 9. The relative deviations between the integral values of the nominal wake at 16.02 kn and 19.95 kn obtained with EFD, DBS, and FSS are 6.84 %, 1.86 %, and 4.62 %, respectively. The relative deviation obtained with FSS at 19.95 kn and 23.94 kn is -9.85 %. The effect of speed is underpredicted with both DBS and FSS at 16.02 kn, even though the results obtained with FSS are in better agreement with those obtained with EFD. As can be seen from Table 9, the integral values of the nominal wake obtained at 16.02 kn are slightly higher than those obtained at 19.95 kn, while the lowest integral value of the nominal wake is obtained at 23.94 kn.

Table 9 Integral values of the nominal wake obtained at different speeds

Speed, kn	$w_{n, EFD}$	$w_{n, DBS}$	$w_{n, FSS}$
16.02	0.375	0.329	0.340
19.95	0.351	0.323	0.325
23.94	/	/	0.293

3.4 Effect of loading condition

In this subsection, the results obtained with CFD and EFD for different loading conditions are presented. The contours of the dimensionless axial velocity component obtained with EFD, DBS, and FSS are shown in Figure 17. It can be seen that smaller velocity reductions are obtained with EFD, DBS, and FSS for the trim angle of -0.5° in comparison to even keel. In the region close to the propeller tip radius, the velocity reductions obtained with EFD are smaller than those obtained with DBS and FSS. On the other hand, the velocity

reductions near the propeller hub obtained by EFD are larger than those obtained numerically. Again, the results obtained with FSS show better agreement with the EFD results. Additional FSS were conducted for trim angles of -0.25°, 0.25°, and 0.5°. The obtained contours of the dimensionless axial velocity component are presented in Figure 18. It can be seen that the velocity reduction over the entire propeller disc plane is smaller, while the wake peak in the region close to 180° is larger as the trim angle increases. Thus, a more favourable flow is obtained for trim by stern than for trim by bow compared to even keel. The velocity reductions close to the propeller hub due to the increase in the trim angle are insignificant.
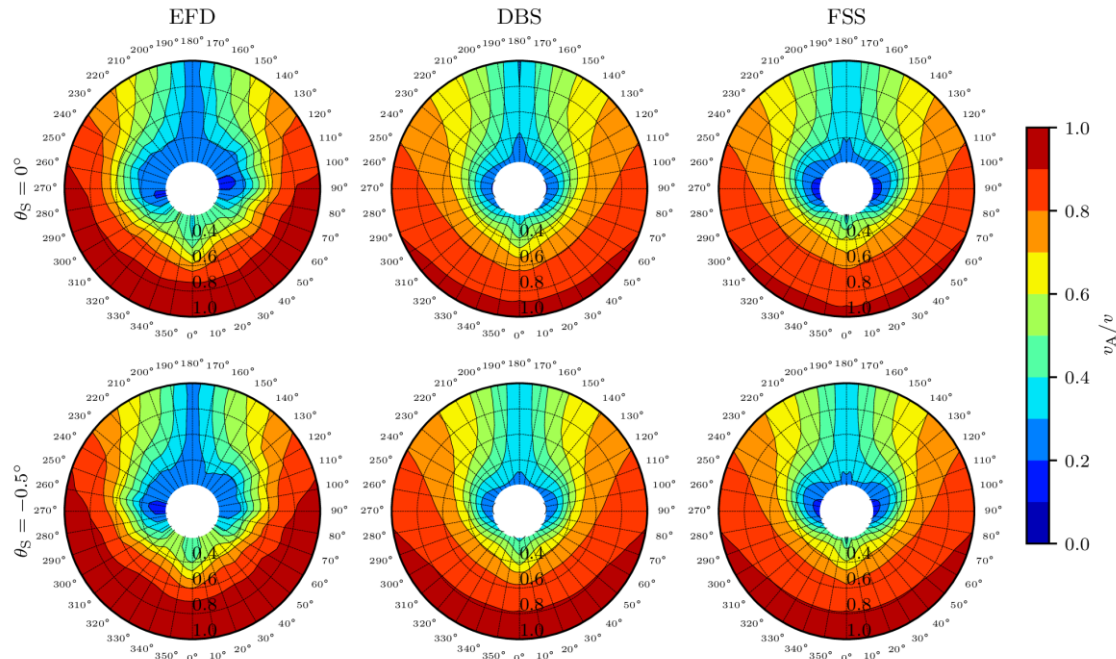
Fig. 17 Contours of the dimensionless axial velocity component on the propeller disc plane obtained with EFD, DBS, and FSS for different loading conditions
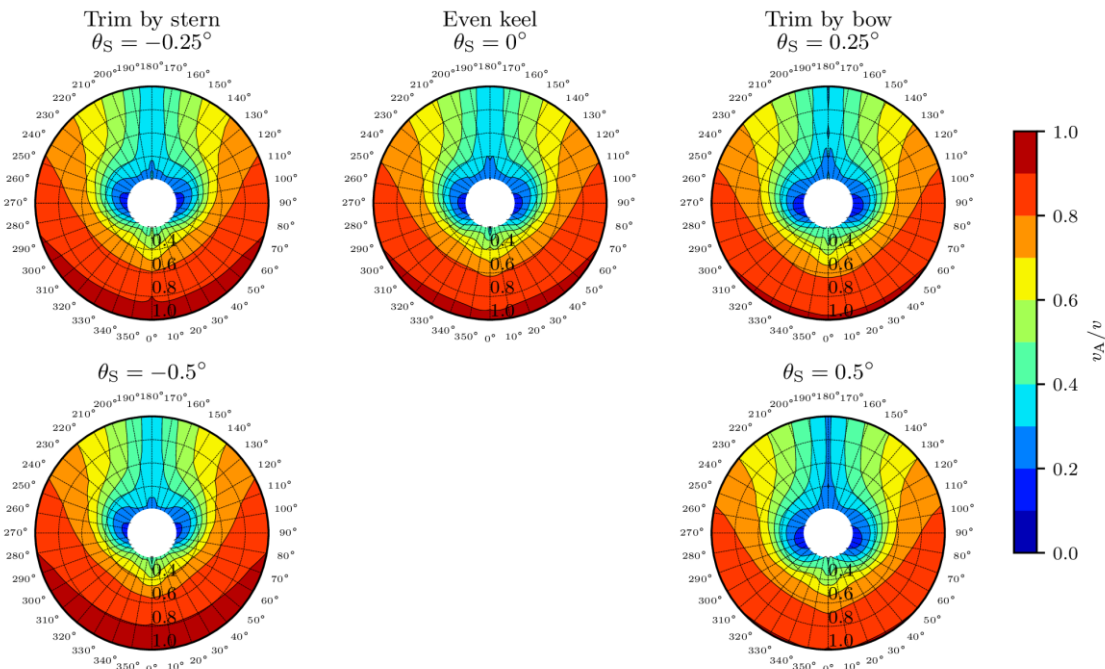
Fig. 18 Contours of the dimensionless axial velocity component on the propeller disc plane obtained with FSS for different loading conditions

19

Figures 19, 20, and 21 show the circumferential distribution of the dimensionless axial, tangential, and radial velocity components, respectively. The effect of the loading condition on the obtained results can be seen in the entire range of radial positions from $0.2R$ to $1.0R$. Higher discrepancies between the results obtained at the investigated loading conditions can be seen at lower radial positions for all velocity components, especially for the axial and tangential velocity components. Lower values of the dimensionless axial and tangential velocity components are obtained for even keel compared to the trim angle of -0.5° in the entire range of the angular positions. On the other hand, the obtained dimensionless radial velocity components are higher for even keel compared to the trim angle of -0.5° at angular positions from 0° to 80° and 280° to 360°. The differences between the dimensionless radial velocity components obtained numerically and by EFD are more pronounced than the other velocity components at all radial positions. The comparison between the circumferential distributions of the axial, tangential, and radial velocity components obtained with FSS for different loading conditions is presented in Appendix B.
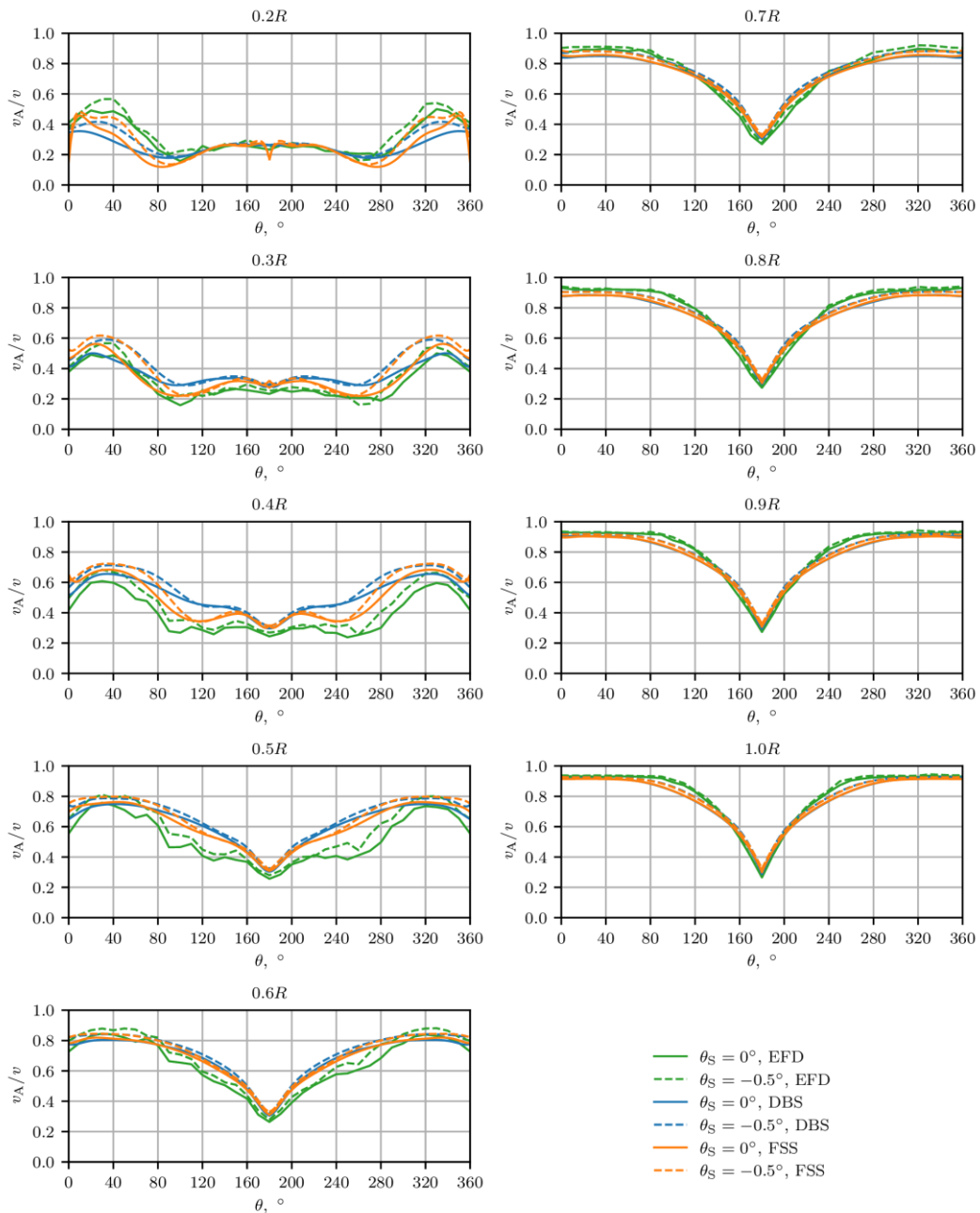

Fig. 19 Circumferential distributions of the axial velocity component for even keel and trim angle of -0.5° at 19.95 kn
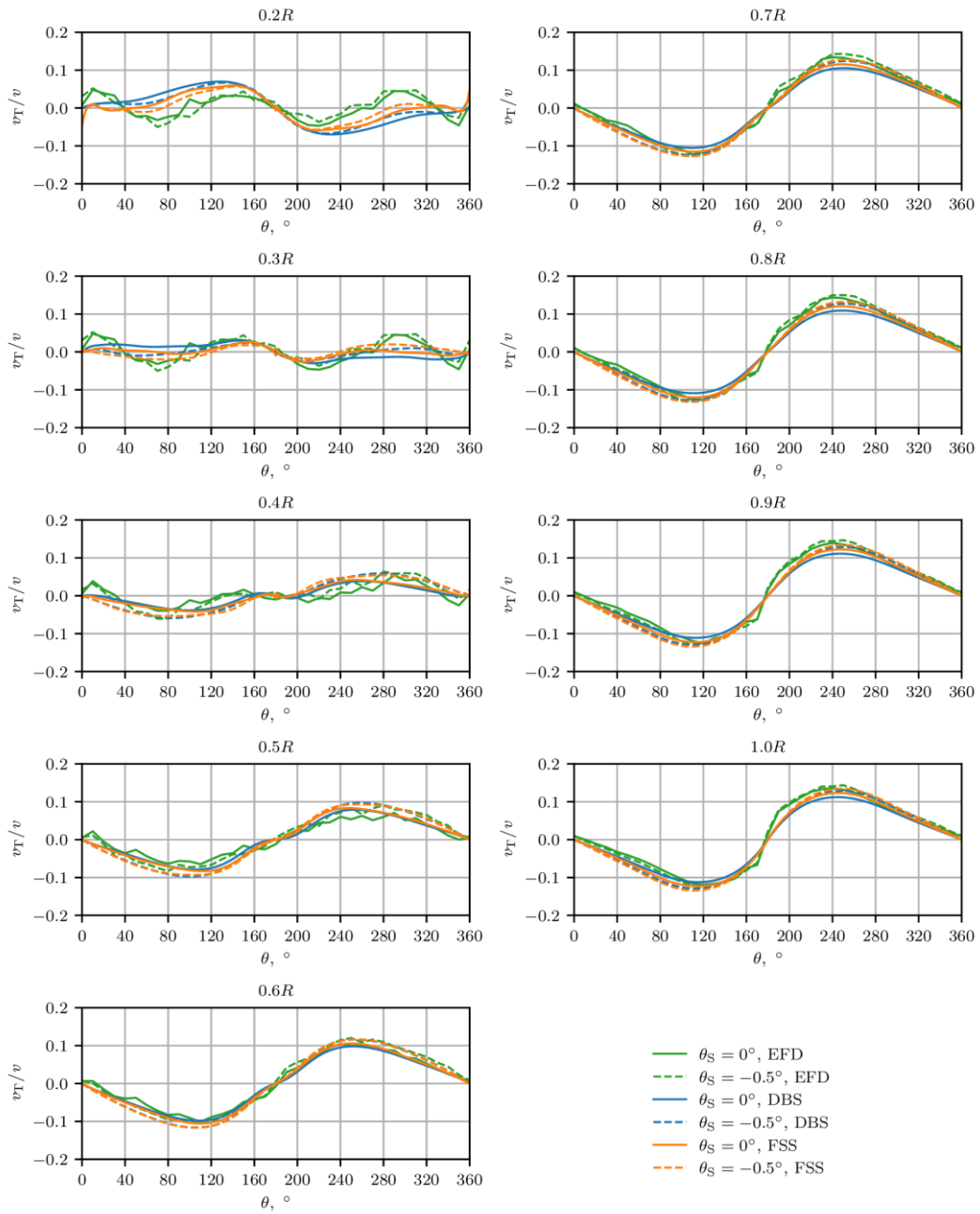
Fig. 20 Circumferential distributions of the tangential velocity component for even keel and trim angle of -0.5° at 19.95 kn
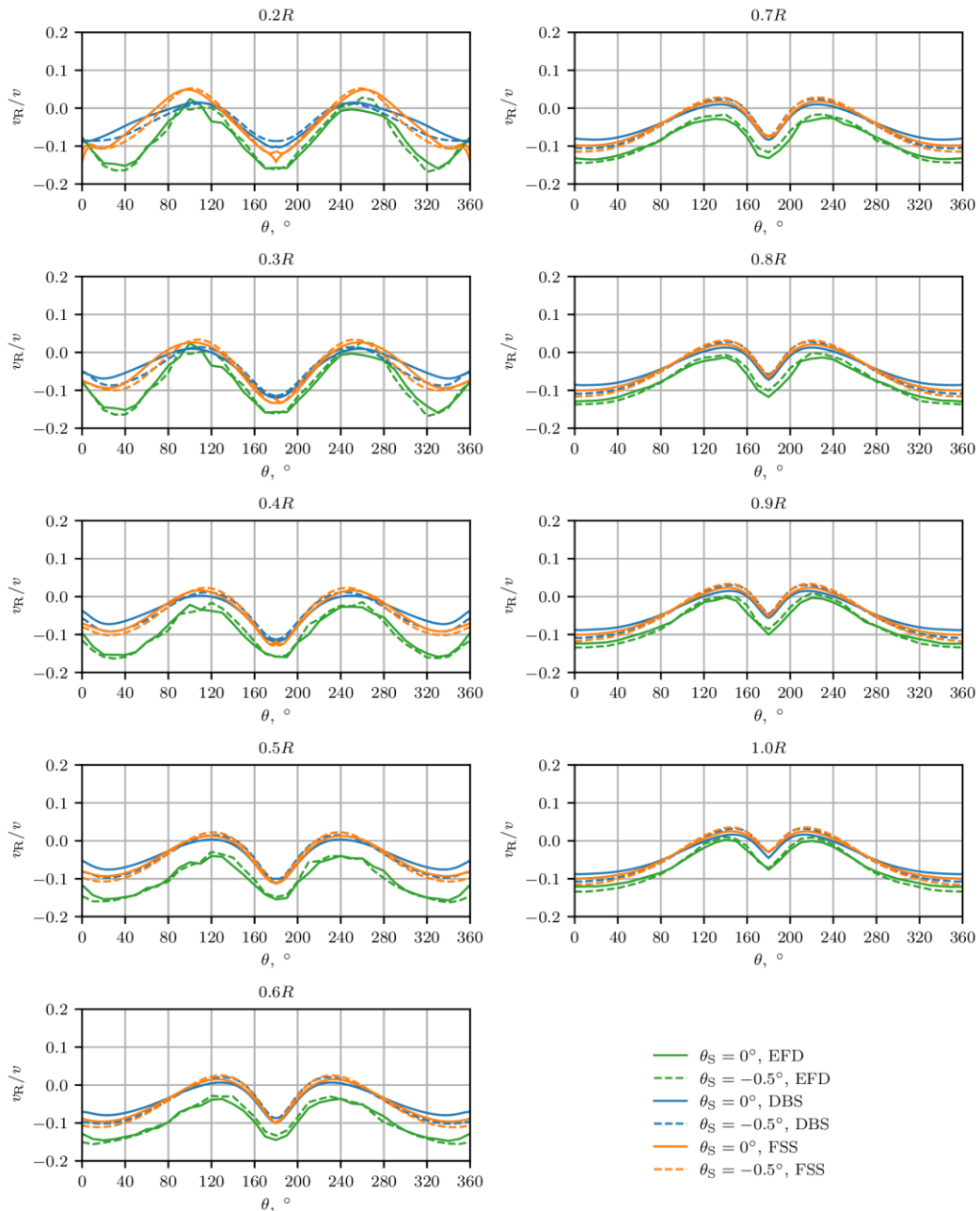
Fig. 21 Circumferential distributions of the radial velocity component for even keel and trim angle of -0.5° at 19.95 kn

Radial distributions of the circumferentially averaged axial velocity component obtained with EFD, DBS, and FSS for even keel and a trim angle of -0.5° are presented in Figure 22. It can be seen that the effect of the loading condition on the circumferentially averaged axial velocity component is significant, with the relative deviations between the results obtained by EFD being up to 11 % at the radial positions $0.4R$ and $0.5R$. The relative deviations between the results obtained numerically are up to 16 % at $0.3R$ for DBS and 15 % at $0.2R$ for FSS. The relative deviations for the analysed loading conditions decrease with the increase of the radius. It should be noted that the relative deviations are calculated with respect to the results obtained for even keel. The circumferentially averaged axial velocity components obtained with FSS for trim angles of -0.5°, -0.25°, 0°, 0.25°, and 0.5° are presented in Figure 23. It can be noticed that the circumferentially averaged axial velocity component decreases with the increase in trim angle over the entire range of the radial positions.
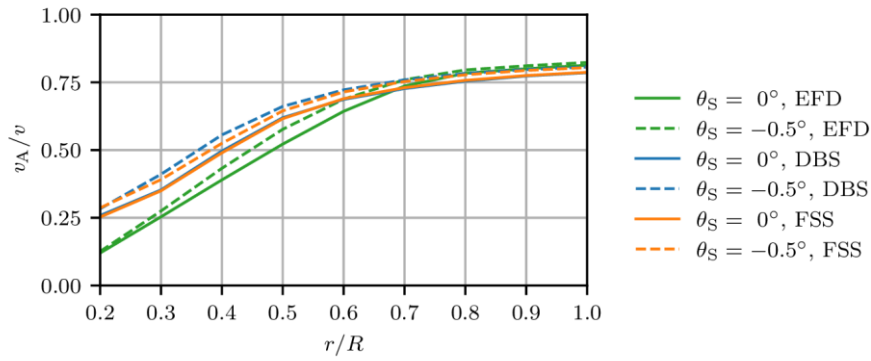
Fig. 22 Radial distributions of the circumferentially averaged dimensionless axial velocity component obtained with EFD, DBS, and FSS for even keel and trim angle of -0.5°
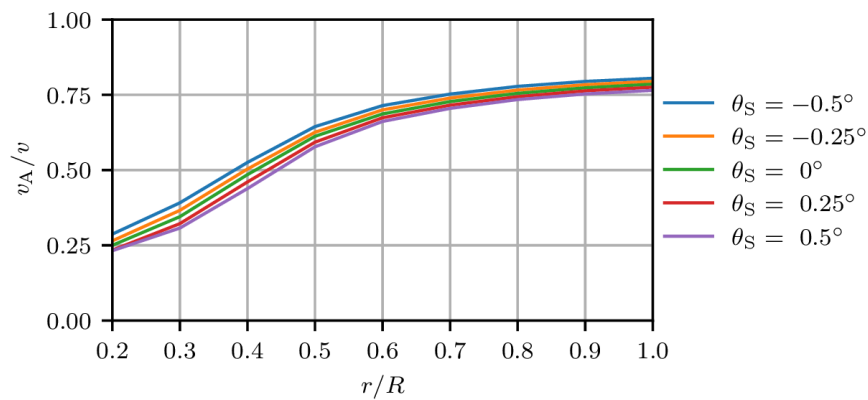

Fig. 23 Radial distributions of the circumferentially averaged dimensionless axial velocity component obtained with FSS for different trim angles

Table 10 Integral values of the nominal wake obtained for even keel and trim angle of -0.5°

	$\theta_S = 0°$	$\theta_S = -0.5°$	RD, %
$w_{n, EFD}$	0.351	0.326	-7.12
$w_{n, DBS}$	0.323	0.288	-10.84
$w_{n, FSS}$	0.325	0.298	-8.31

Table 11 Integral values of the nominal wake obtained with FSS for different trim angles

θ_S, °	$w_{n, FSS}$	RD, %
-0.5	0.298	-8.31
-0.25	0.313	-3.69
0	0.325	/
0.25	0.339	4.31
0.5	0.351	8.00

Table 10 shows the obtained integral values of the nominal wake for different loading conditions. The largest effect of the loading condition on the integral value of the nominal wake is predicted by DBS for a trim angle of -0.5°, with a relative deviation of -10.84 %, while the smallest effect is predicted by EFD with a relative deviation of -7.12 %. The effect of the loading condition is overpredicted with DBS and FSS, even

though the results obtained with FSS are in better agreement with those obtained with EFD. As can be seen from Table 11, the integral values of the nominal wake obtained with FSS increase with the increase in trim angle. The largest relative deviation of -8.31 % is obtained between the trim angle of -0.5° and even keel.

4. Conclusions and future work

The focus of this study is the assessment of the effects of speed and loading conditions on the nominal wake of a Post Panamax 6750 TEU containership. The analysis is carried out based on the measurements from the towing tank and the results of the numerical simulations. The presented results include the contours and the radial distributions of the dimensionless axial velocity component as well as the circumferential distributions of the axial, tangential, and radial velocity components determined at different radial positions, and the integral values of the nominal wake. The results obtained with DBS were compared with those obtained using FSS. Based on this study, the following conclusions are drawn:

- Relative deviations between the numerically and experimentally obtained circumferentially averaged dimensionless axial velocity component decrease with the increase of the radius. The dimensionless axial velocity component obtained numerically is overpredicted at radial positions from $0.2R$ to $0.7R$, and slightly underpredicted above $0.7R$. The results obtained with FSS show slightly better accordance with the EFD results than those obtained with DBS. The velocity reductions obtained numerically are larger than those obtained experimentally in the entire propeller disc plane, except in the region close to the propeller hub.

- A larger wake peak in the region close to 180° at a speed of 16.02 kn is obtained by EFD in comparison to 19.95 kn. The results obtained with FSS show that the velocity reduction over the entire propeller disc plane is smaller as the ship speed increases, which was not captured entirely by DBS. The differences between the dimensionless radial velocity components obtained numerically and by EFD are more pronounced than the other velocity components. A slight effect of speed on the axial velocity component can be seen at radial positions closer to the propeller hub for DBS and FSS. The differences between the dimensionless axial velocity components obtained at 16.02 kn and 19.9 kn with EFD can be seen at all the radial positions. Only a slight effect of speed on the circumferentially averaged axial velocity is observed. The effect of speed is more noticeable for the results obtained with EFD in comparison to the numerically obtained results, which is especially pronounced for the integral value of the nominal wake.

- Smaller reductions of the dimensionless axial velocity component are obtained for a trim angle of -0.5° in comparison to even keel with both EFD and CFD. The effect of the loading condition can be noticed in the obtained circumferential distributions of all velocity components. The effect of the loading condition on the circumferentially averaged dimensionless axial velocity component is more pronounced at radial positions closer to the propeller hub. Similar results are seen for the circumferentially averaged axial velocity for which the relative deviations between the results obtained numerically are up to 16 % at $0.3R$ for DBS and 15 % at $0.4R$ for FSS with respect to the results obtained for even keel. The relative deviations for the considered loading conditions decrease with the increase in radius. The integral value of the nominal wake obtained by FSS increases with the increase in trim angle. The largest effect of the loading condition on the integral value of the nominal wake is obtained with DBS with a relative deviation of -10.84 % between a trim angle of -0.5° and even keel. The results obtained with FSS are in better agreement with those obtained with EFD.

This study provides valuable experimental data for CFD benchmark studies as well as numerical results for the nominal wake obtained using DBS and FSS at the model scale. Future studies will focus on the assessment of the scale effects on the ship propulsion characteristics, which will include an assessment of the scale effects on the nominal wake. This will be a step further in the improvement of the existing extrapolation procedures for the nominal wake.

A. Appendix

Figures A1-A3 show the circumferential distributions of the dimensionless axial, tangential, and radial velocity components at radial positions from $0.2R$ to $1.0R$, obtained with FSS at different speeds.
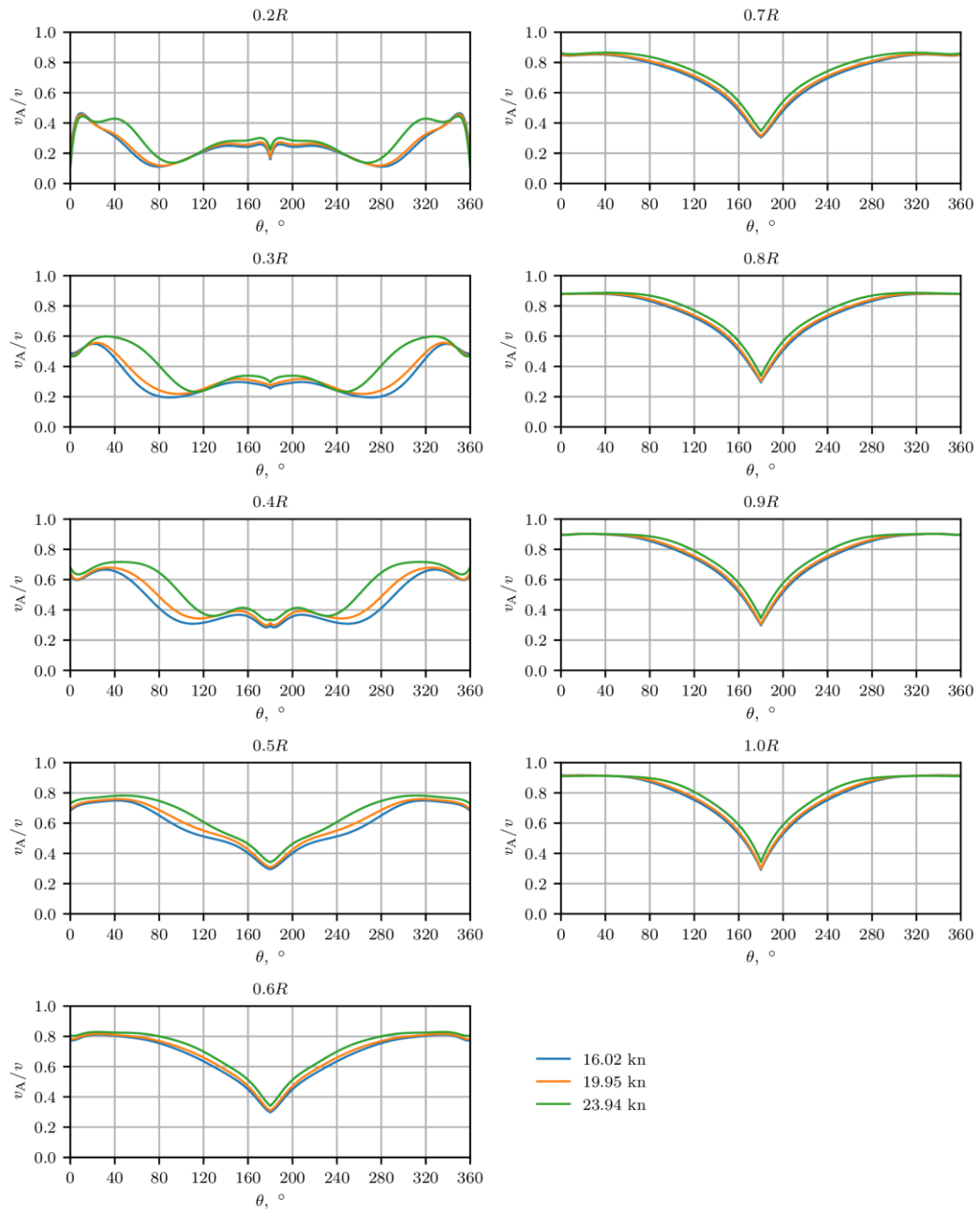

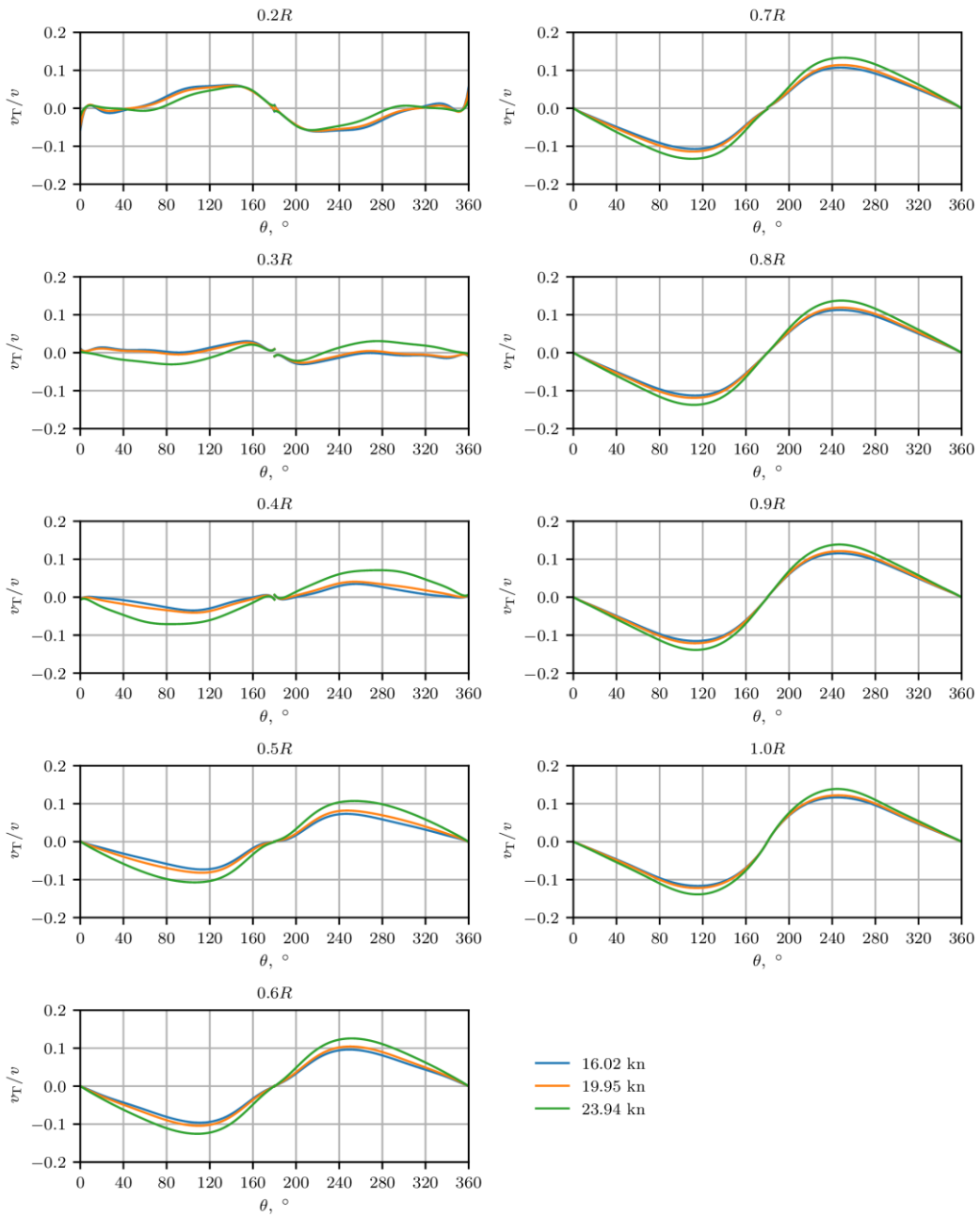**Fig. A1** Circumferential distributions of the axial velocity component obtained with FSS at different speeds

Fig. A2 Circumferential distributions of the tangential velocity component obtained with FSS at different speeds
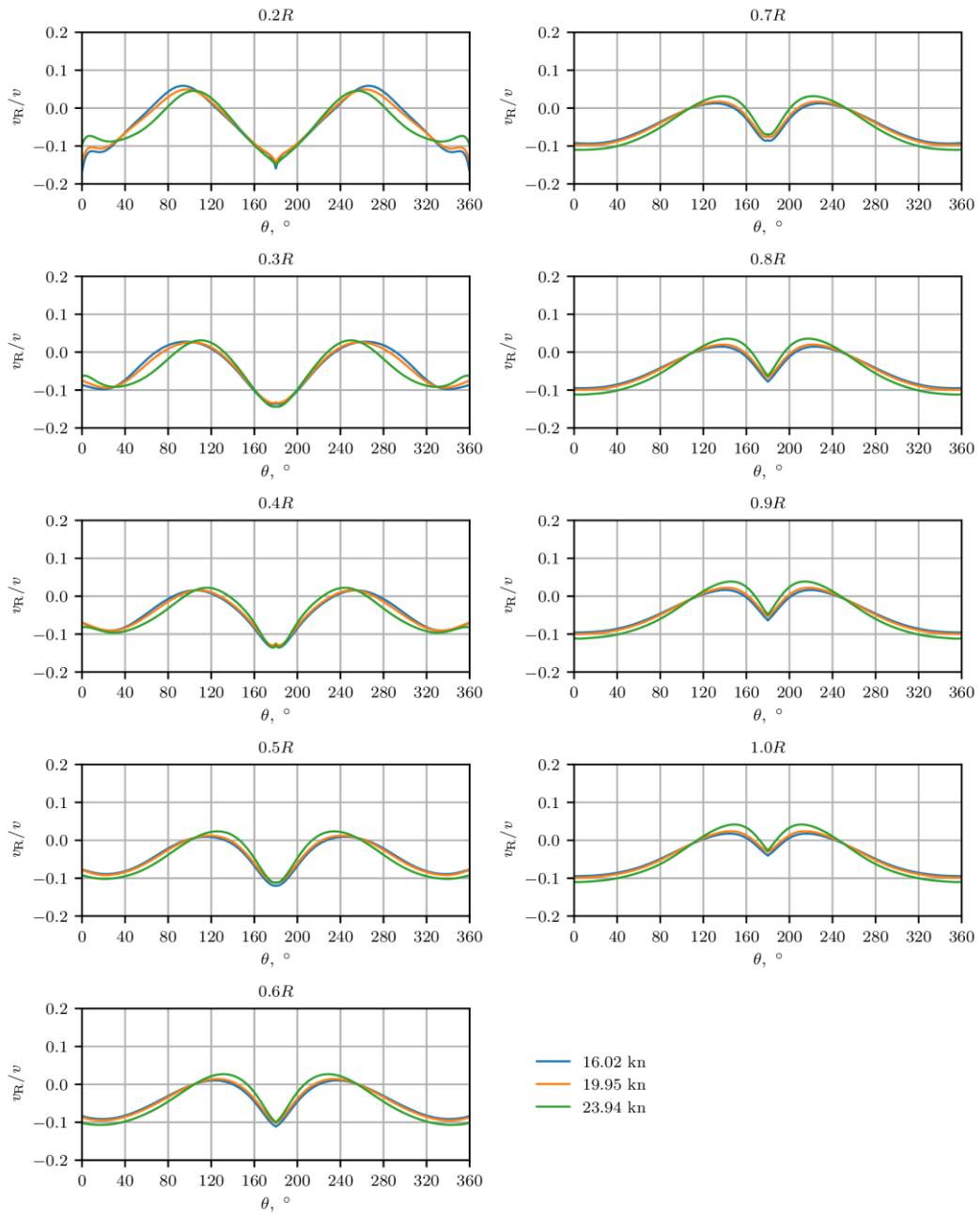
Fig. A3 Circumferential distributions of the radial velocity component obtained with FSS at different speeds.

B. Appendix

Figures B1-B3 show the circumferential distributions of the dimensionless axial, tangential, and radial velocity components at radial positions from $0.2R$ to $1.0R$, obtained with FSS for different loading conditions.
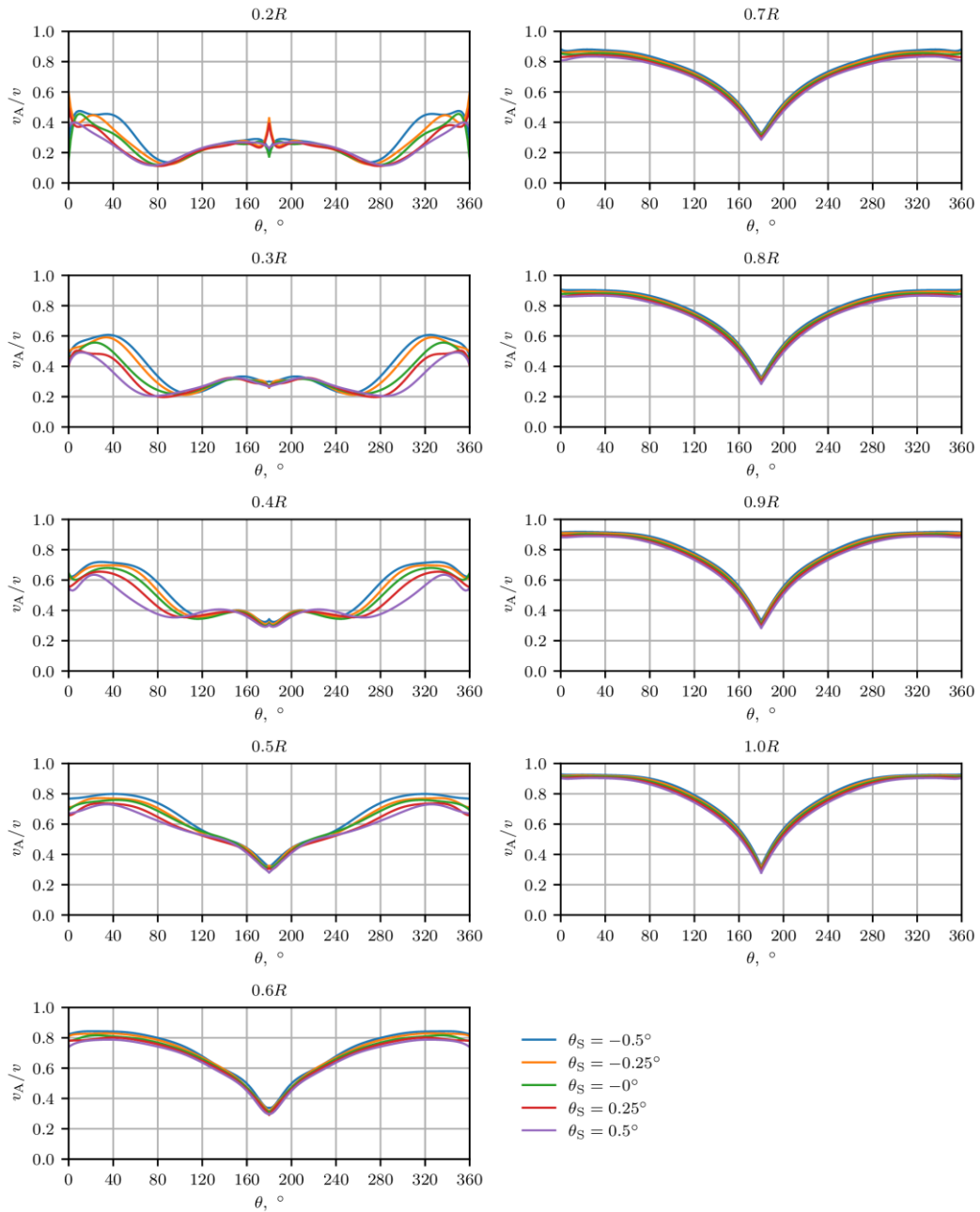

Fig. B1 Circumferential distributions of the axial velocity component obtained with FSS for different loading conditions
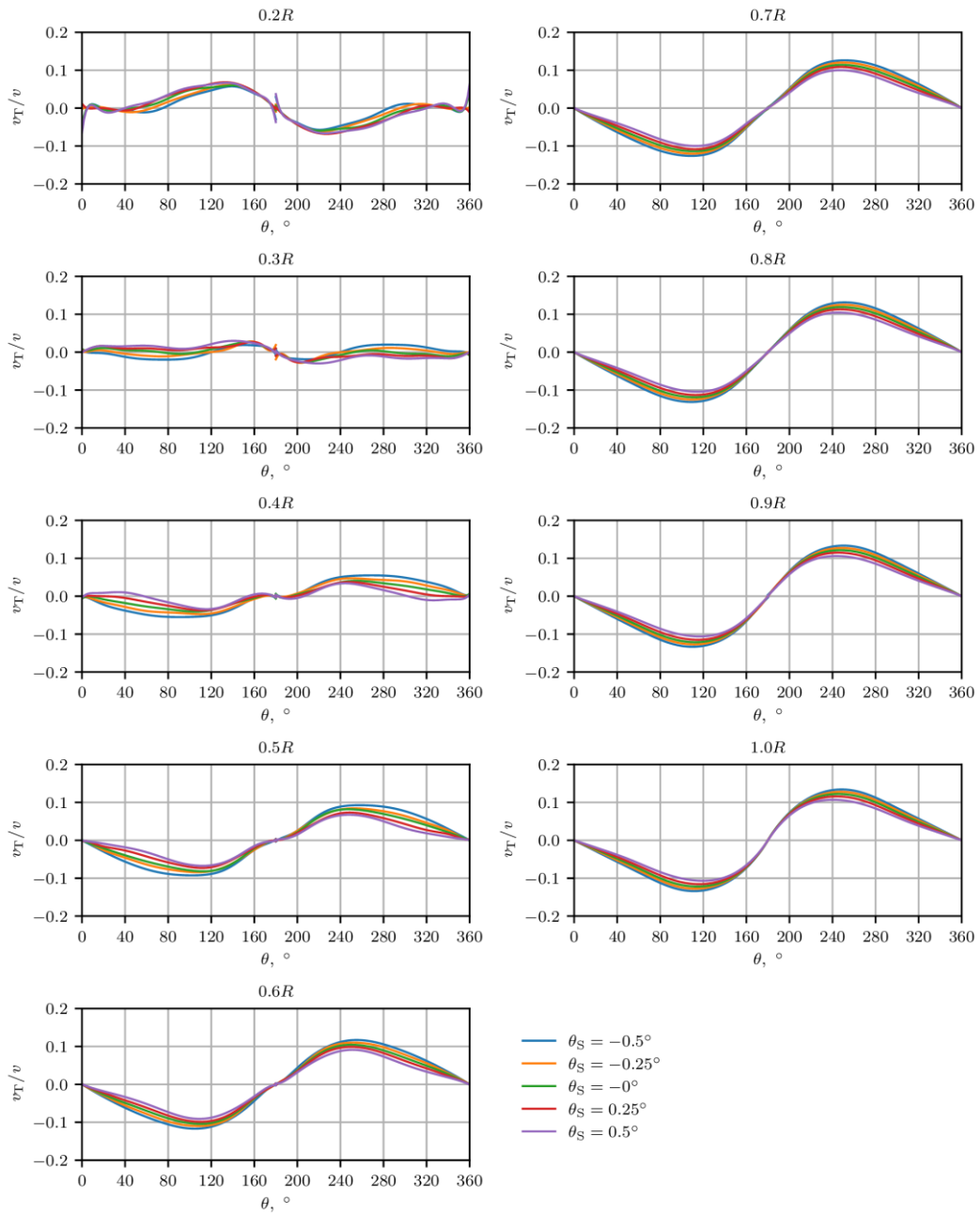
Fig. B2 Circumferential distributions of the tangential velocity component obtained with FSS for different loading conditions
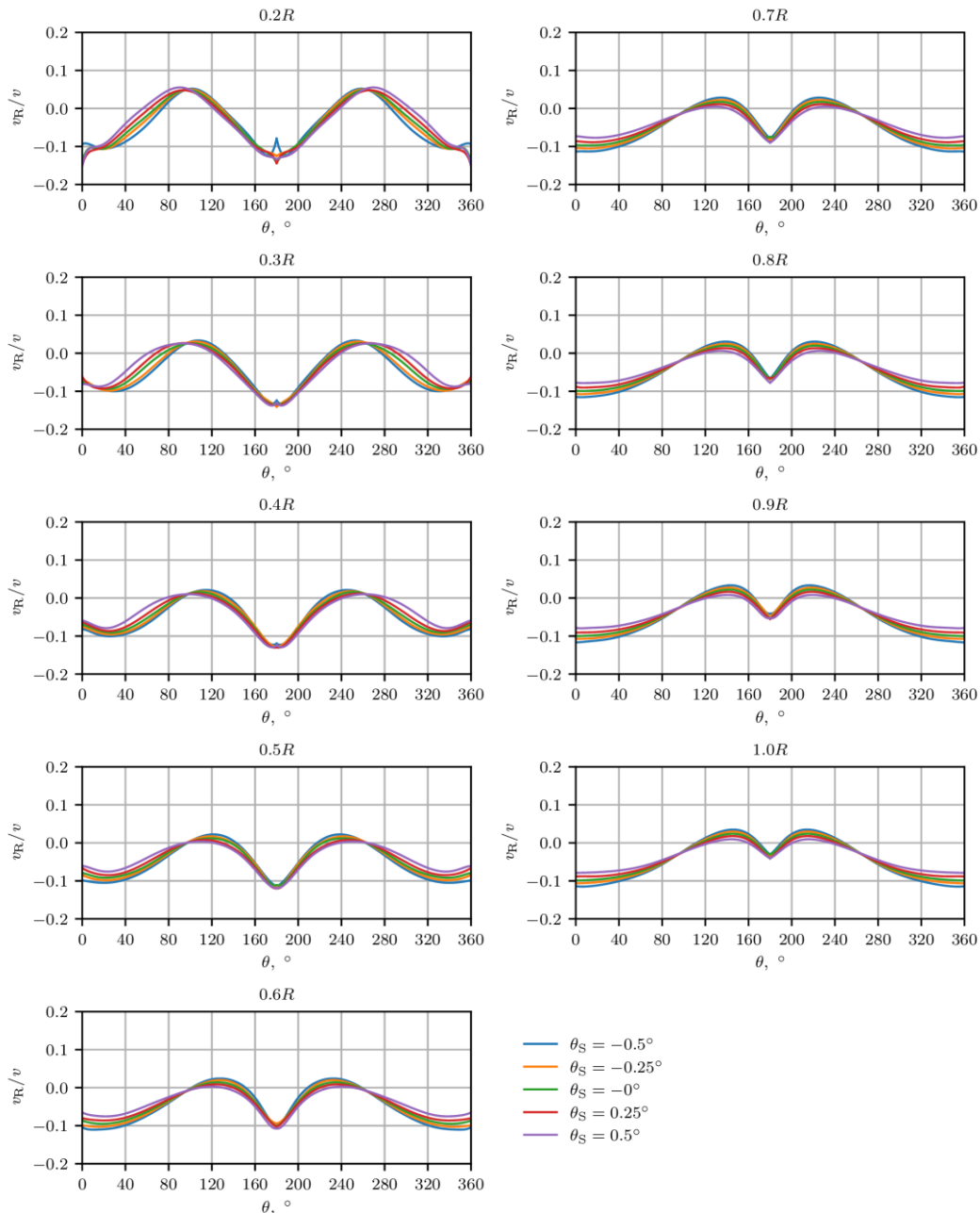
Fig. B3 Circumferential distributions of the radial velocity component obtained with FSS for different loading conditions

FUNDING

ACKNOWLEDGEMENTS

REFERENCES

[1] Park, S., Oh, G., Rhee, S. H., Koo, B. Y., Lee, H., 2015. Full scale wake prediction of an energy saving device by using computational fluid dynamics. *Ocean Engineering*, 101, 254–263. https://doi.org/10.1016/j.oceaneng.2015.04.005

[2] Regener, P., Mirsadraee, Y., Andersen, P., 2018. Nominal vs. effective wake fields and their influence on propeller cavitation performance. *Journal of marine science and technology*, 6(2), 34. https://doi.org/10.3390/jmse6020034

[3]   Farkas, A., Degiuli, N., Martić, I., Dejhalla, R., 2019. Numerical and experimental assessment of nominal wake for a bulk carrier. *Journal of marine science and technology*, 24, 1092–1104. https://doi.org/10.1007/s00773-018-0609-4

[4]   Zhang, Y. X., Lai, M. Y., Ni, Y. G., Feng, L., 2021. CFD study of hull wakes in oblique flow at model and full scales. *Applied Ocean Research*, 112, 102689. https://doi.org/10.1016/j.apor.2021.102689

[5]   Dogrul, A., Song, S., Demirel, Y. K., 2020. Scale effect on ship resistance components and form factor. *Ocean Engineering*, 209, 107428. https://doi.org/10.1016/j.oceaneng.2020.107428

[6]   Pena, B., Muk-Pavic, E., Fitzsimmons, P., 2020a. Detailed analysis of the flow within the boundary layer and wake of a full-scale ship. *Ocean Engineering*, 218, 108022. https://doi.org/10.1016/j.oceaneng.2020.108022

[7]   Pena, B., Muk-Pavic, E., Thomas, G., Fitzsimmons, P., 2020b. An approach for the accurate investigation of full-scale ship boundary layers and wakes. *Ocean Engineering*, 214, 107854. https://doi.org/10.1016/j.oceaneng.2020.107854

[8]   Liu, J. Z., Zou, Z. J., Guo, H. P., Chen, C. Z., 2023. A study on the interaction among hull, engine and propeller during self-propulsion of a ship. *Ocean Engineering*, 286, 115702. https://doi.org/10.1016/j.oceaneng.2023.115702

[9]   Dogrul, A., 2022. Numerical prediction of scale effects on the propulsion performance of Joubert BB2 submarine. *Brodogradnja*, 73(2), 17–42.

[10]   Sakamoto, N., Kobayashi, H., Ohashi, K., Kawanami, Y., Windén, B., Kamiirisa, H., 2020. An overset RaNS prediction and validation of full scale stern wake for 1,600TEU container ship and 63,000 DWT bulk carrier with an energy saving device. *Applied Ocean Research*, 105, 102417. https://doi.org/10.1016/j.apor.2020.102417

[11]   Farkas, A., Degiuli, N., Martić, I., 2021. The impact of biofouling on the propeller performance. *Ocean Engineering*, 219, 108376. https://doi.org/10.1016/j.oceaneng.2020.108376

[12]   Farkas, A., Degiuli, N., Martić, I., 2020. Impact of biofilm on the resistance characteristics and nominal wake. *Proceedings of the Institution of Mechanical Engineers, Part M: Journal of Engineering for the Maritime Environment*, 234, 59–75. https://doi.org/10.1177/1475090219862897

[13]   Wang, Z. Z., Xiong, Y., Wang, R., Shen, X. R., Zhong, C. H., 2015. Numerical study on scale effect of nominal wake of single screw ship. *Ocean Engineering*, 104, 437–451. https://doi.org/10.1016/j.oceaneng.2015.05.029

[14]   Shin, H. W., Paik, K. J., Jang, Y. H., Eom, M. J., Lee, S., 2020. A numerical investigation on the nominal wake of KVLCC2 model ship in regular head waves. *International Journal of Naval Architecture and Ocean Engineering*, 12, 270–282. https://doi.org/10.1016/j.ijnaoe.2020.01.001

[15]   Mikkelsen, H., Shao, Y., Walther, J. H., 2022. Numerical study of nominal wake fields of a container ship in oblique regular waves. *Applied Ocean Research*, 119, 102968. https://doi.org/10.1016/j.apor.2021.102968

[16]   Dai, K., Li, Y., Gong, J., Fu, Z., Li, A., Zhang, D., 2022. Numerical study on propulsive factors in regular head and oblique waves. *Brodogradnja*, 73(1), 37–56. https://doi.org/10.21278/brod73103

[17]   Farkas, A., Degiuli, N., Martić, I., 2017. Numerical simulation of viscous flow around a tanker model. *Brodogradnja*, 68(2), 109–125. https://doi.org/10.21278/brod68208

[18]   Sun, W., Hu, Q., Hu, S., Su, J., Xu, J., Wei, J., Huang, G., 2020. Numerical analysis of full-scale ship self-propulsion performance with direct comparison to statistical sea trail results. *Journal of Marine Science and Engineering*, 8(1), 24. https://doi.org/10.3390/jmse8010024

[19]   Guo, C., Wu, T., Zhang, Q., Luo, W., Su, Y., 2017. Numerical simulation and experimental studies on aft hull local parameterized non-geosim deformation for correcting scale effects of nominal wake field. *Brodogradnja*, 68(1), 77–96. https://doi.org/10.21278/brod68105

[20]   Can, U., Delen, C., Bal, S., 2020. Effective wake estimation of KCS hull at full-scale by GEOSIM method based on CFD. *Ocean Engineering*, 218, 108052. https://doi.org/10.1016/j.oceaneng.2020.108052

[21]   Kim, Y., Kim, J. H., 2016. Benchmark study on motions and loads of a 6750-TEU containership. *Ocean Engineering*, 119, 262–273. https://doi.org/10.1016/j.oceaneng.2016.04.015

[22]   Brodarski Institute, 2022. Report 6652-M. resistance, self-propulsion and 3D wake measurement test results. *Brodarski Institute*.

[23]   Siemens, 2020. STAR-CCM+ User Guide.

[24]   ITTC, 2017. Practical guidelines for RANS calculation of nominal wakes ITTC.

[25]   Choi, J., Yoon, S. B., 2009. Numerical simulations using momentum source wave-maker applied to RANS equation model. *Coastal Engineering*, 56, 1043–1060. https://doi.org/10.1016/j.coastaleng.2009.06.009

[26]   ITTC, 2011. Practical guidelines for ship CFD applications, 7.5-03-02-03. *ITTC-Recommended Procedures and Guidelines*.

[27]   Grlj, C. G., Degiuli, N., Martić, I., 2023. The impact of numerical parameters on the resistance characteristics of a container ship at the model and full scale. *Journal of Marine Science and Engineering*, 11(9), 1672. https://doi.org/10.3390/jmse11091672

[28]   Mikulec, M., Piehl, H., 2023. Verification and validation of CFD simulations with full-scale ship speed/power trial data. *Brodogradnja*, 74(1), 41–62. https://doi.org/10.21278/brod74103

[29]   Celik, I. B., Ghia, U., Roache, P. J., Freitas, C. J., Coleman, H., Raad, P.E., 2008. Procedure for estimation and reporting of uncertainty due to discretization in CFD applications. *ASME. Journal of Fluids Engineering*, 130, 078001. https://doi.org/10.1115/1.2960953

[30]   Eça, L., Hoekstra, M., 2014. A procedure for the estimation of the numerical uncertainty of CFD calculations based on grid refinement studies. *Journal of Computational Physics*, 262, 104–130. https://doi.org/10.1016/j.jcp.2014.01.006